

THESIS FOR THE DEGREE OF DOCTOR OF PHILOSOPHY


Characterisation and modelling of graphene FET detectors for  
flexible terahertz electronics

XINXIN YANG

Terahertz and Millimetre Wave Laboratory  
Department of Microtechnology and Nanoscience - MC2  
CHALMERS UNIVERSITY OF TECHNOLOGY

Göteborg, Sweden 2020

**Characterisation and modelling of graphene FET detectors for flexible terahertz electronics**

XINXIN YANG  <https://orcid.org/0000-0003-4464-6922>

ISBN 978-91-7905-265-2

© XINXIN YANG, 2020

Doktorsavhandlingar vid Chalmers tekniska högskola  
Ny serie nr. 4732  
ISSN 0346-718X

Chalmers University of Technology  
Department of Microtechnology and Nanoscience - MC2  
Terahertz and Millimetre Wave Laboratory  
SE-412 96 Göteborg, Sweden  
Phone: +46(0)31 772 1000

Cover:

On-wafer terahertz characterisation (bottom left), a single-pixel antenna integrated GFET terahertz detector (top left), and a set of linear arrays on plastic substrate (right)

Printed by Chalmers Reproservice  
Göteborg, Sweden March 2020

# Abstract

Low cost electronics for future high-speed wireless communication and non-invasive inspection at terahertz frequencies require new materials with advanced mechanical and electronic properties. Graphene, with its unique combination of flexibility and high carrier velocity, can provide new opportunities for terahertz electronics. In particular, several types of power sensors based on graphene have been demonstrated, and found suitable as fast and sensitive detectors over a wide part of the electromagnetic spectrum. Nevertheless, the underlying physics for signal detection are not well understood due to the lack of accurate characterisation methods, which hampers further improvement and optimisation of graphene-based power sensors. In this thesis, progress on modelling, design, fabrication and characterisation of terahertz graphene field effect transistor (GFET) detectors is presented. A major part is devoted to the first steps towards flexible terahertz electronics.

The characterisation and modelling of terahertz GFET detectors from 1 GHz to 1.1 THz are presented. The bias dependence, the scattering parameters and the detector voltage response were simultaneously accessed. It is shown that the voltage responsivity can be accurately described using a combination of a quasi-static equivalent circuit model, and the second-order series expansion terms of the nonlinear dc  $I - V$  characteristic. The video bandwidth, or IF bandwidth, of GFET detectors is estimated from heterodyne measurements. Moreover, the low-frequency noise of GFET detectors between 1 Hz and 1 MHz is investigated. From this, the room-temperature Hooge parameter of fabricated GFETs is extracted to be around  $2 \times 10^{-3}$ . It is found that the thermal noise dominates above 100 Hz, which sets the necessary switching time to reduce the effect of  $1/f$  noise.

A state-of-the-art GFET detector at 400 GHz, with a maximum measured optical responsivity of 74 V/W, and a minimum noise-equivalent power of  $130 \text{ pW}/\sqrt{\text{Hz}}$  is demonstrated. It is shown that the detector performance is affected by the quality of the graphene film and adjacent layers, hence indicating the need to improve the fabrication process of GFETs.

As a proof of concept, a bendable GFET terahertz detector on a plastic substrate is demonstrated. The effects of bending strain on dc  $I - V$  characteristics, responsivity and sensitivity are investigated. The detector exhibits a robust performance for tensile strain of more than 1% corresponding to a bending radius of 7 mm. Finally, a linear array of terahertz GFET detectors on a flexible substrate for imaging applications is fabricated and tested. The results show the possibility of realising bendable and curved focal plane arrays.

In summary, in this work, the combination of improved device models and more accurate characterisation techniques of terahertz GFET detectors will allow for further optimisation. It is shown that graphene can open up for flexible terahertz electronics for future niche applications, such as wearable smart electronics and curved focal plane imaging.

**Keywords:** terahertz detectors, graphene, field-effect transistors, flexible electronics, sensors, arrays, broadband characterisation, scattering parameters.



# List of publications

## Appended papers

This thesis is based on the following papers:

- [A] **Xinxin Yang**, Andrei Vorobiev, Kjell Jeppson, and Jan Stake, “Describing broadband terahertz response of graphene FET detectors by a classical model”, *IEEE Transactions on Terahertz Science and Technology*, vol. 10, no. 2, 2020. DOI: 10.1109/TTHZ.2019.2960678
- [B] **Xinxin Yang**, Andrei Vorobiev, Kjell Jeppson, Jan Stake, Luca Banszerus, Christoph Stampfer, Martin Otto, and Daniel Neumaier, “Wide bandwidth terahertz mixers based on graphene FETs”, in *44th International Conference on Infrared, Millimeter, and Terahertz Waves (IRMMW-THz)*, Paris, France, 2019. DOI: 10.1109/IRMMW-THz.2019.8873869
- [C] **Xinxin Yang**, Andrei Vorobiev, Kjell Jeppson, Jan Stake, Luca Banszerus, Christoph Stampfer, Martin Otto, and Daniel Neumaier, “Low-frequency noise characterization of graphene FET THz detectors”, in *43rd International Conference on Infrared, Millimeter, and Terahertz Waves (IRMMW-THz)*, Nagoya, Japan, 2018. DOI: 10.1109/IRMMW-THz.2018.8510404
- [D] Andrey A. Generalov, Michael A. Andersson, **Xinxin Yang**, Andrei Vorobiev, and Jan Stake, “A 400-GHz graphene FET detector”, *IEEE Transactions on Terahertz Science and Technology*, vol. 7, no. 5, pp. 614–616, July 2017. DOI: 10.1109/TTHZ.2017.2722360
- [E] **Xinxin Yang**, Marlene Bonmann, Andrei Vorobiev, Kjell Jeppson, and Jan Stake, “Test structures for evaluating Al<sub>2</sub>O<sub>3</sub> dielectrics for graphene field effect transistors on flexible substrates”, in *2018 IEEE International Conference on Microelectronic Test Structures (ICMTS)*, Austin, TX, USA, 2018, pp. 75-78. DOI: 10.1109/ICMTS.2018.8383768

- [F] **Xinxin Yang**, Andrei Vorobiev, Andrey A. Generalov, Michael A. Andersson, and Jan Stake, “A flexible graphene terahertz detector”, *Applied Physics Letters*, vol. 111, no. 2, pp. 021102-1–021102-4, July 2017. DOI: 10.1063/1.499 3434
- [G] **Xinxin Yang**, Andrei Vorobiev, Jian Yang, Kjell Jeppson, and Jan Stake, “A linear-array of 300-GHz antenna integrated GFET detectors on a flexible substrate”, submitted as a Letter to *IEEE Transactions on Terahertz Science and Technology*, February, 2020.

# Abbreviations

**AFM** atomic force microscope. 10

**ALD** atomic layer deposition. 25

**BOE** buffered oxide etchant. 21, 23

**CL** conversion loss. 33

**CMOS** complementary metal-oxide-semiconductor. 22, 44

**CVD** chemical vapour deposition. 2, 21, 22, 49, 51

**EBL** electron-beam lithography. 24

**FET** field-effect transistor. 8, 9

**GFET** graphene field-effect transistor. 2, 3, 9, 11, 12, 15, 16, 25, 27, 37, 43

**GSG** ground–signal–ground. 29

**h-BN** hexagonal boron nitride. 43

**HBD** heterojunction backward diode. 40, 44

**HEMT** high-electron-mobility transistor. 1, 9, 40, 44

**IoT** Internet of things. 43

**MOSFET** metal-oxide semiconductor field-effect transistor. 1, 11, 40

**NEP** noise equivalent power. 1, 2, 39, 41

**PDMS** polydimethylsiloxane. 25

**PEN** polyethylene naphthalate. 23, 40

**PET** polyethylene terephthalate. 23, 24, 39

**PI** polyimide. 25

**PMMA** polymethyl methacrylate. 25

**PTFE** polytetrafluoroethylene. 39, 40

**THz** terahertz. 1

**VNA** vector network analyzer. 29

# Notations

- $C_{\text{gs}}$  source-gate capacitance. 9
- $C_{\text{G}}$  gate capacitance per unit area. 28
- $L$  gate length. 18, 28
- $P_{\text{ava}}$  available input signal power. 17
- $P_{\text{in}}$  input signal power. 5
- $R_{\text{DS}}$  source-drain resistance. 28
- $R_{\text{D}}$  parasitic drain resistance. 9
- $R_{\text{S}}$  parasitic source resistance. 9
- $T$  temperature. 7
- $T_{\text{gl}}$  glass transition temperature. 23, 24
- $V_{\text{Dir}}$  gate voltage of the Dirac point. 28
- $W$  gate width. 18, 28
- $\Delta U$  the power of input RF signal. 5
- $\Gamma$  reflection coefficient. 18
- $\alpha$  fine structure constant. 10
- $\alpha_H$  Hooge parameter. 7
- $\hbar$  Planck's constant. 28
- $\mathfrak{R}_V$  detector voltage responsivity. 6, 31
- $\mu$  carrier mobility. 7, 28
- $\sigma$  electrical conductivity. 12
- $k_B$  Boltzmann's constant. 7, 12
- $n_0$  residual carrier density of graphene. 28
- $n_{\text{G}}$  carrier density induced by gate voltage. 28
- $q$  electron charge. 28
- $r_{\text{ds}}$  intrinsic source-drain resistance. 9
- $v_{\text{F}}$  Fermi velocity. 28



# Contents

<b>Abstract</b>	<b>i</b>
<b>List of publications</b>	<b>iii</b>
<b>Abbreviations</b>	<b>v</b>
<b>Nomenclature</b>	<b>v</b>
<b>1 Introduction</b>	<b>1</b>
<b>2 Background</b>	<b>5</b>
2.1 Terahertz detectors . . . . .	5
2.2 FET detectors . . . . .	8
2.3 GFET terahertz detectors . . . . .	9
<b>3 GFET terahertz detector modelling and design</b>	<b>15</b>
3.1 Classical nonlinear electrical model for GFET detection . . . . .	15
3.2 Design of GFET power detectors . . . . .	17
3.3 Design of planar antennas . . . . .	18
<b>4 Fabrication of GFET detectors</b>	<b>21</b>
4.1 Fabrication process flow of GFET detectors . . . . .	21
4.2 Graphene growth and transfer . . . . .	22
4.3 Substrates . . . . .	23
4.4 Ohmic contact . . . . .	24
4.5 Gate dielectric . . . . .	25
<b>5 On-wafer characterisation of GFET detectors</b>	<b>27</b>
5.1 DC characterisation . . . . .	27
5.2 Scattering parameter characterisation . . . . .	29
5.3 RF power detector characterisation . . . . .	30
5.4 IF bandwidth characterisation . . . . .	33
5.5 Low-frequency noise characterisation . . . . .	34
<b>6 Antenna-integrated GFET terahertz detectors</b>	<b>37</b>
6.1 Free-space terahertz detection setup . . . . .	37
6.2 GFET detector . . . . .	37
6.3 GFET detector on flexible substrate . . . . .	39
6.4 GFET detector array on flexible substrate . . . . .	40
<b>7 Conclusions and future outlook</b>	<b>43</b>

Summary of appended papers	45
Appendix	49
Bibliography	55
Acknowledgements	67
Appended papers	69

# Chapter 1

## Introduction

The terahertz (THz) radiation lies between microwaves and the optical region of the electromagnetic spectrum, often defined as the frequency range from 0.3-10 THz [1]. For long time, astronomical observation [2] has been the main driver for development of terahertz technology. However, over the past few decades, terahertz science and technology [3, 4] have being exploited for many applications in biomedical sensing and imaging [5], noninvasive inspection [6], security screening [7] and wireless communication [8]. Common to all these systems and instruments is the need to detect and monitor the signal intensity with a power sensor [9].

The photon energy of the terahertz radiation ( $h\nu = 4.1$  meV at 1 THz) is relatively low compared to radiation at much shorter infrared, visible and UV wavelengths. Moreover, the output power of terahertz transmitters is usually weak due to the difficulty of generating strong terahertz signals, often referred to as the terahertz gap [10]. For passive sensor applications, the detector measures the natural emitted power from an object according to Planck's law of radiation. In this case, terahertz detectors with high-sensitivity are particularly important [9]. Superconducting detectors [11] can provide high sensitivity, but usually operate at cryogenic temperatures with relatively complex cooling systems, whereas nonlinear semiconductor devices, such as Schottky diodes and transistors, can be used as fast and sensitive detectors at room temperature. For comparison, the noise equivalent power (NEP), a figure of merit for sensitivity, of different kinds of terahertz detectors operating at room temperature is shown in Figure 1.1. The NEP of a zero bias Schottky diode is reported to be  $5 - 20$  pW/ $\sqrt{\text{Hz}}$  at  $600 - 900$  GHz [12]. Transistor detectors with a sensitivity in the range of  $10 - 30$  pW/ $\sqrt{\text{Hz}}$  up to 900 GHz have been demonstrated based on different semiconductors including heterojunction bipolar transistor [13], metal-oxide semiconductor field-effect transistor (MOSFET) [14] and high-electron-mobility transistor (HEMT) [15]. However, with the recent rapid expansion of terahertz science and technology, the existing rigid and bulky solutions are not able to meet the need for future novel applications, such as wearable smart electronics and Internet of things, which call for flexible, portable, less expensive and eco-friendly solutions. In the MHz and GHz frequency range, flexible sensors [16] and communication devices [17] have been embedded into clothing or other textiles. In 2016, Suzuki et al. demonstrated the first flexible and wearable terahertz scanner based on carbon nanotubes [18]. However, this technique is largely limited by the low sensitivity of carbon nanotube detectors. Moreover, there is a need for large focal plane detector arrays [19] with the ability to integrate and conform to any surface [20].

Graphene, a two-dimensional material with extraordinary electrical and mechanical properties [34], is a promising candidate for high-frequency electronics, such as detectors [35], mixers [36] and modulators [37] in the terahertz frequency range. The recent progress

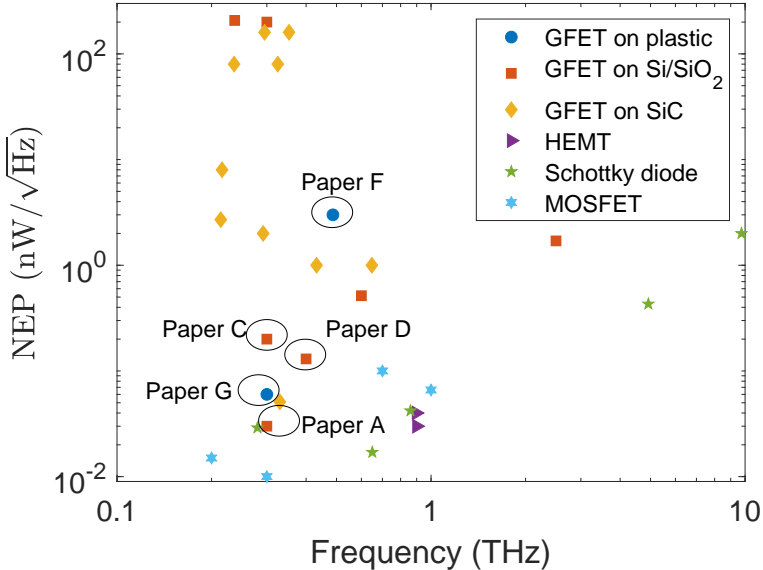


Figure 1.1: Terahertz power sensors. A comparison of estimated NEP for GFET detector in Paper [A, C, D, F and G] and reported data in Ref. [21, 22, 23, 15, 24, 25] as well as other types of detectors: Schottky diode [26, 27], HEMT [28, 29, 30], and MOSFET [14, 31, 32, 33].

in high-quality and large-area growth of graphene films shows the feasibility of large-scale fabrication graphene devices on plastic substrates [17, 16]. In 2012, Vicarelli et al. [22] demonstrated the first exfoliated graphene field-effect transistor (GFET) terahertz detector on Si/SiO<sub>2</sub> substrate, with NEP of 200 nW/√Hz and 30 nW/√Hz at 300 GHz for monolayer and bilayer devices, respectively. This work was followed up by Zak et al. in 2014 demonstrating an estimated NEP of 515 pW/√Hz at 600 GHz using chemical vapour deposition (CVD) graphene [21]. By reducing the residual carrier density of graphene, a 400-GHz GFET detector with NEP of 130 pW/√Hz is demonstrated in [Paper E]. Using an antenna-integrated graphene pn-junction, a NEP of 80 pW/√Hz is obtained in the frequency range of 1.8–4.2 THz [38]. Excellent performance has also been achieved by GFET detectors on SiC substrate [15]. Furthermore, an flexible GFET detector is first reported in Paper F with NEP below 3 nW/√Hz, and the first GFET detector array on plastic substrate has been demonstrated in Paper G. However, the performance of GFET detectors is still lower than that of other types of nonlinear semiconductor detectors.

To exploit the full potential of GFET detectors, a better understanding of device principles and the main limiting factors are important. Many researchers have considered contributions of plasma wave mixing [22], thermoelectric [39] and bolometric effects [40], or nonlinearity of the dc  $I - V$  characteristics [41], to explain detection mechanisms and corresponding modelling at terahertz frequencies [42]. However, the lack of accurate

characterisation techniques at terahertz frequencies has hampered the development of device models. By accurate and comprehensive on-wafer characterisation and modelling in Paper A, it shows that GFET direct power detection can be described over a wide frequency range by the nonlinear carrier transport characteristic obtained at static electrical fields.

In this doctoral thesis, research on modelling, design, fabrication and characterisation of terahertz detectors based on GFET is presented in the following six chapters. Chapter 2 presents challenges in terahertz detection by comparing different terahertz detection mechanisms and devices, and provides an overview of flexible electronics, graphene properties and GFET characteristics. Chapter 3 provides a detailed description of GFET terahertz detection modelling and the design of antennas and detectors. Chapter 4 describes state-of-the-art processing technologies for high-performance GFET detectors on both rigid and flexible substrates. Chapter 5 presents the on-wafer measurement setup and characterisation results of GFET power detectors. Chapter 6 presents the quasi-optical setup and the characterisation results of antenna-integrated GFET terahertz detectors and detector arrays. Chapter 7 summarises the results of this thesis and provides a future outlook.



# Chapter 2

## Background

Terahertz detectors [9] are key components for many applications [43, 19]. This chapter provides an overview of basic operation principles and figures of merit of terahertz direct power detectors. In addition, different types of detectors will be presented and discussed, including a more detailed description of FET detectors. Finally, theoretical potential and practical limitations of GFETs for terahertz detection will be presented.

### 2.1 Terahertz detectors

Terahertz detectors can be divided into direct and heterodyne detectors. Figures 2.1 (a) and (b) illustrate the basic operations of a direct power detector and a heterodyne detector. The direct power detector is used to convert a fraction of incoming signal to a dc voltage or current. The heterodyne detector, often called mixer, is used to translate an RF signal to intermediate frequency by mixing with another signal. If the RF signal and LO frequencies are equal, the IF degenerates to dc - a detection process called homodyne conversion.

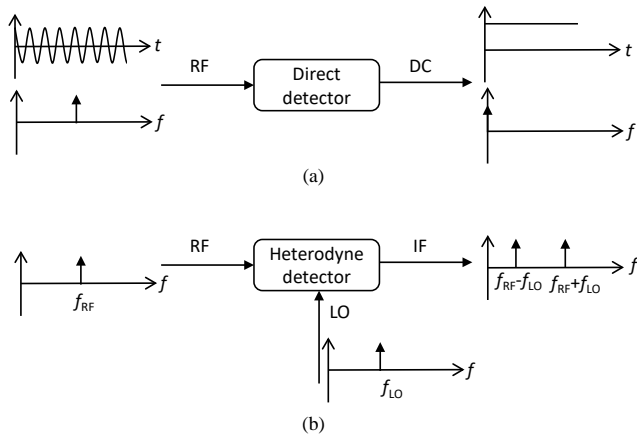


Figure 2.1: Basic operations of a direct power detector and a heterodyne detector.

Figure 2.2 shows the relation between the output rectified dc voltage ( $\Delta U$ ) and the power of input RF signal ( $P_{in}$ ) of a power detector. At very low input power levels, the rectified dc voltage is dominated by the noise generated by the detector, which defines

the noise floor. For a linear, or square law detector, the rectified dc voltage is directly proportional to the power of input RF signal. With the increase of the input power, the rectified dc voltage will saturate, which means that the read-out signal no longer increases linearly with the input power. The difference between the noise floor and the compression point defines the dynamic range of a power detector.

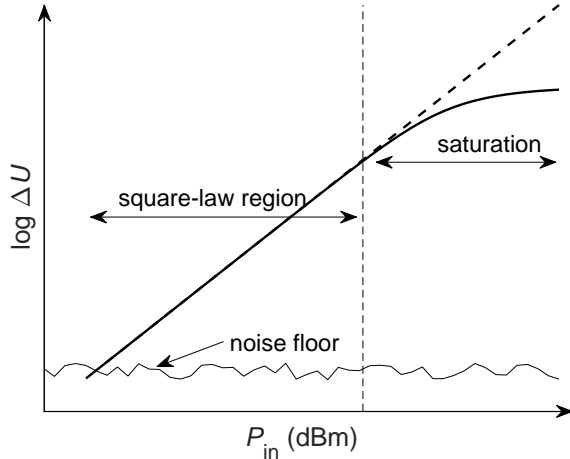


Figure 2.2: Illustrating the dynamic range of a power detector.

An important figure of merit is the voltage responsivity ( $\mathfrak{R}_V$ ), which is defined as the slope of the rectified dc readout signal versus signal power, and can be defined as

$$\mathfrak{R}_V = \frac{dU}{dP_{in}} \approx \frac{\Delta U}{P_{in}}. \quad (2.1)$$

The sensitivity of a power detector, usually expressed by NEP, is an important figure of merit for characterising the minimum detectable input signal power, which is given by

$$\text{NEP} = \frac{\sqrt{S_V}}{\mathfrak{R}_V}. \quad (2.2)$$

where  $S_V$  is the noise spectral density.

For many terahertz applications, such as radiometers and passive imaging, signal power is often very weak and close to the noise floor. The internally generated noise in a detector is usually caused by random motions of charges. The different physical noise sources are used to categorise the different type of noise as:

- *Thermal noise*, also known as Johnson or Nyquist noise, arises from the thermal agitation of charges inside a conductor. The thermal current noise spectral density is given by Nyquist's formula [44],

$$S_I(f) = \frac{4k_B T}{R}, \quad (2.3)$$



where  $f$  is the frequency,  $R$  is the resistance,  $k_B k_B$  is the Boltzmann's constant and  $T$  is the temperature.

- *Shot noise* originates from the discrete nature of the electric charge and the random emission or capture of carriers [45]. Assuming a Poisson distribution, Schottky was able to describe the shot noise as,

$$S_I(f) = 2q \langle I \rangle, \quad (2.4)$$

where  $\langle I \rangle$  is the average value of the electrical current. With a low or zero-drain-source bias, the shot noise is negligible. Note that both thermal and shot noise have their origin in the random motion of charge carriers. Due the frequency independency, they are called white noise.

- *Flicker noise* varies inversely with frequency, and is hence often called  $1/f$  noise. In contrast with other types of intrinsic noise,  $1/f$  noise can originate from different fluctuation processes either in the charge carrier number ( $N$ ), mobility ( $\mu$ ), or from both. A common example is generation-recombination noise causing a low frequency fluctuation of charge carrier numbers. For electronic devices, the empirical model by Hooge [46] can be used to describe the spectral density as

$$\frac{S_V(f)}{V^2} = \frac{S_I(f)}{I^2} = \frac{\alpha_H}{fN}, \quad (2.5)$$

where  $\alpha_H$  is the Hooge parameter which is the most commonly used figure of merit for  $1/f$  noise. The value of the Hooge parameter can be very different for different materials and structures [47].

Although the sensitivity and response time are very important figure-of-merits of a power detector, the ultimate measurement uncertainty of a detector is set by the stability. The drift will limit the integration time, and thereby the standard deviation of the power measurement. The stability and accuracy can be characterised by measuring the Allan variance [48] versus integration time. The variance will improve with integration time until systematic errors or drift dominates.

Based on different physical phenomena, most terahertz detectors can be classified into three broad categories, i.e. thermal detectors, photo detectors and nonlinear semiconductor detectors.

Thermal detectors utilize temperature-dependent physical properties of materials. In a thermal detector, the incident radiation is absorbed to heat the material, which results in changes of material properties that used to generate an electrical output. Depending on different kinds of temperature-dependent physical properties, thermal detectors can be further sub-divided into three types including:

- *Bolometers*. For a bolometer, the power of incident radiation is measured by heating a material which has a temperature-dependent resistance [49]. Bolometers can be made of different kinds of materials, including superconductors, semiconductors, and metals. Superconducting and semiconducting bolometers can provide high sensitivity at cryogenic temperatures [11]. However, the cooling systems are complex and

expressive. Room-temperature bolometers, thermally isolated on thin membranes based on  $\text{VO}_x$ , have been shown to operate in a wide frequency range, but with a typical response time of several milliseconds.

- *Pyroelectric detectors.* A pyroelectric detector is based on a thin ferroelectric crystal, e.g.  $\text{LiTaO}_3$ , which has a temperature-dependent dielectric constant. Pyroelectric detectors are sensitive, typically used at room temperature and have a broad, flat spectral response across most of the electromagnetic spectrum. The incident radiation signal for pyroelectric detectors must be chopped or modulated at less than 100 Hz.
- *Calorimetric sensors.* A calorimetric sensor is based on measuring the temperature rise of a well-matched metal film by the resistance change with the absorption of incident radiation. It is used to measure power over a wide frequency. However, the response time of calorimetric sensors [50] is usually low, especially with low input power, and the drift is relatively large.
- *Golay cells.* A Golay cell is based on thermal absorption in a gas-filled chamber and a detected change in volume via a displaced mirror in an optical amplifier. Golay cells work at ambient temperatures and have broad spectral response. In 2009, the study of Desmaris et al. has shown that the Golay cell promises a bandwidth of 3.5 THz (0.5 – 4 THz) [51]. However, they are very slow in the terahertz response and can not be used for high-speed terahertz detection.

The second class of detectors are photo detectors [52]. A typical example is the superconductor-insulator-superconductor detector, which operates at cryogenic temperatures with very high sensitivity.

The last class of detectors are nonlinear semiconductor detectors based on different types of diodes and transistors, such as Schottky-barrier diode [53, 54], backward tunnel diode [55], heterojunction bipolar transistor [56] and field-effect transistor (FET) [57] (see details about FET detectors in the next section). The detector responsivity is directly related to the nonlinearity of  $I - V$  characteristics. This type of detector are fast and operate at room temperature. They are commonly used in both direct power detection and heterodyne detection systems.

## 2.2 FET detectors

The use of FETs as direct power detectors was first demonstrated based on GaAs HEMTs by Krekels et al. in 1992 [58]. The detection of FETs is based on the nonlinear I-V characteristics of transistors, which leads to a rectification of the RF input signal. As a result, a dc voltage (or current) response appears between source and drain, being proportional to the RF signal power. Since the mid-90s, development of broadband terahertz detectors based on FETs has been a target of intensive theoretical and experimental studies [59, 33, 60, 61]. FET detectors have been successfully implemented in different material systems including: Si, GaN/AlGaIn [62], GaAs/AlGaAs [63].

The equivalent circuit of a FET is shown in Figure 2.3. The intrinsic FET, inside the dashed-line rectangle, is surrounded by external parasitic resistances, i.e.  $R_G$ ,  $R_D$  and  $R_S$ , parasitic capacitances i.e.  $C_{PG}$ ,  $C_{PD}$  and  $C_{DS}$ , and parasitic inductances (i.e.  $L_G$ ,  $L_D$  and  $L_S$ ). The values of the equivalent circuit elements can be derived from measured S-parameters through fitting or direct parameter extraction techniques [64, 65, 66].

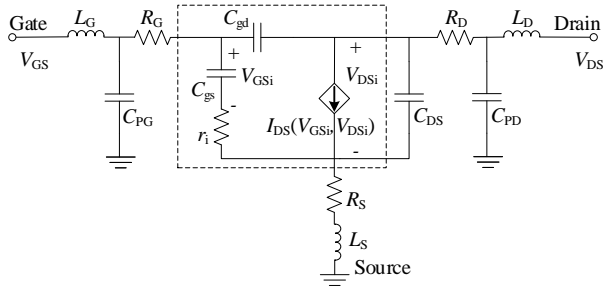


Figure 2.3: Equivalent circuit of a FET.

As an important figure of merit for FET and diode detectors, the cut-off frequency of a FET detector derived by Anderson et al. [41] can be expressed as,

$$f_{3dB} \approx \frac{1}{2\pi C_{gs} \sqrt{r_{ds} R_S}}, \quad (2.6)$$

where  $r_{ds}$  is the intrinsic source-drain resistance,  $C_{gs}$  is the source-gate capacitance, and  $R_S$  is the parasitic source resistances.

## 2.3 GFET terahertz detectors

Graphene, a two-dimensional sheet of carbon atoms arranged in a honeycomb lattice, was first produced and identified in 2004, by Andre Geim and Konstantin Novoselov team [34]. In 2010, they were awarded the Nobel Prize in physics for their pioneering research on graphene. The impressive electrical and mechanical properties of graphene have opened up new horizons for flexible high-frequency electronics.

Since 2012, Vicarelli et al. demonstrated the first FET terahertz detector [22], much work has been done in the area of GFET terahertz detection. Although GFET detectors exhibit lower sensitivity than Schottky diode detectors and HEMT detectors, GFETs have shown great promise and potential as sensitive terahertz detectors. Furthermore, taking advantage of graphene with its excellent mechanical properties, GFET are expected to play an important role in the future development of flexible terahertz technology.

### Graphene properties

In 1947, Wallace first analysed the band structure of monolayer graphene by using the tight-binding approach [67]. The band structure of large-area graphene is shown in Figure

2.4. The valence and conduction bands are cone shaped and meet at the Dirac points of the Brillouin zone. Due to the zero bandgap, the graphene channel cannot be switched off totally.

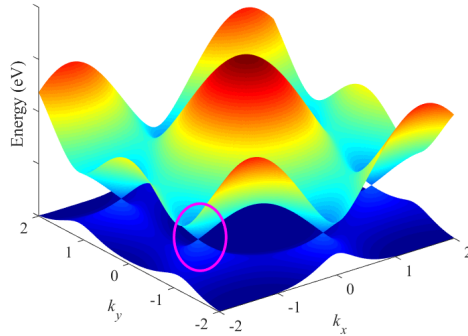


Figure 2.4: Graphene band structure.

Carrier mobility and saturation velocity describe the carrier transport in low and high electric fields, respectively. The linear dispersion relationship close to one of the Dirac points indicates two-dimensional massless electrons in graphene, which represents the origin of the superior carrier mobility in ideal graphene. The carrier mobility has been demonstrated greater than  $2 \times 10^5 \text{ cm}^2/\text{Vs}$  at 5 K in suspended monolayer graphene fabricated by exfoliation [68]. However, a substrate and a gate dielectric are typically required in real applications. The presence of charge carrier scattering limits the electron mean free path and leads to degradation of the mobility, which is a major barrier in the development progress of graphene based devices. The carrier velocity in graphene at high fields does not drop as drastically as that in III-V semiconductors [69]. The maximum values of carrier velocity for graphene devices is approximately  $4 \times 10^7 \text{ cm/s}$ , compared with a value of  $2 \times 10^7 \text{ cm/s}$  for GaAs and  $10^7 \text{ cm/s}$  for silicon.

The mechanical properties of graphene are controlled by the characteristics of ideal pristine crystal lattices and structural defects (e.g. grain boundaries). Lee et al. conducted the first systematic experimental analysis of the elastic properties and intrinsic strength of free-standing monolayer graphene membranes by nanoindentation in an atomic force microscope (AFM) [70]. The results have shown that Young's modulus and third-order elastic stiffness of monolayer graphene is 1.0 TPa and -2.0 TPa, respectively. Brittle fracture of graphene occurs at a critical stress equal to its intrinsic strength of 130 GPa. Furthermore, graphene sheets can sustain stretching as large as 20%. These values are considerably larger than those of all other materials, and stimulate great interest in applying graphene for various applications.

The optical properties of graphene are determined by direct interband electron transitions that can be modulated by an external gate field [71]. The light transmittance ( $T$ ) through free-standing graphene with a universal optical conductance of  $G_0 = e^2/4\hbar$  can be derived using Fresnel equations as  $T = (1 + \pi\alpha)^{-2} \approx 0.977$ , where  $\alpha$  is the fine structure

constant [72]. Thus, the transition and absorption coefficients of monolayer graphene are 97% and 2.3%, respectively, which are independent of the wavelength [72]. The graphene-light interaction is strong. The electron-hole pairs generated by photo-excitation in graphene can be separated by built-in electric fields of metal/graphene contacts, which can be used as the basis of graphene photodetectors [73, 74].

## Graphene field-effect transistor

Since the field effect in graphene was reported by Novoselov et al. in 2004 [34], considerable efforts have been devoted to developing high-performance GFETs [75]. A schematic of a GFET with source, drain, and gate terminals is shown in Figure 2.5.

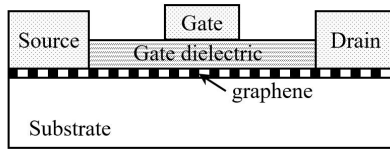


Figure 2.5: Device schematic of a GFET.

The operation of GFETs relies on controlling the drain current by the gate voltage. As shown in Figure 2.6, in contrast with MOSFET, both the carrier density and the type of carriers in the graphene channel are governed by the potential differences between the channel and the gate, whereas MOSFETs turn off below a certain threshold voltage. Large positive and negative gate voltages promote an n-type channel and a p-type channel, respectively, which leads to the two branches of the transfer characteristics separated by the Dirac point. The position of the Dirac point is defined by charged impurities in the dielectric and at the interface between the dielectric and the graphene.

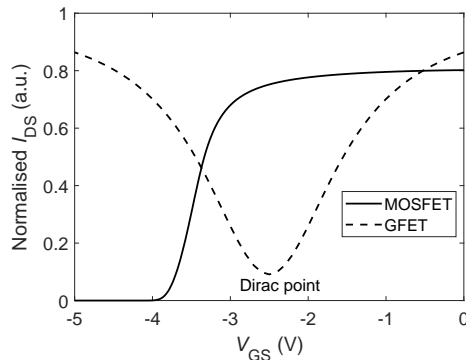


Figure 2.6: MESFET and GFET transfer characteristics.

## Detection mechanisms

Several different mechanisms of GFET terahertz detection have been proposed. These include the photovoltaic effect, the photo-thermoelectric model and the plasma model:

- The *photovoltaic effect* is caused by excitation of an electron or other charge carrier to a higher-energy state. In 2009, V. Ryzhii first theoretically analysed the graphene bilayer phototransistor for terahertz detection and infrared detection by the photovoltaic effect [76]. The negative bias of the top gate results in a depletion in the graphene. This forms the potential barrier for electrons, which controls the injected electron current from the source to the drain. With terahertz radiation, the electron-hole pairs are generated in the depleted section. The photo-generated electrons move out of the depleted section, while the photo-generated holes are accumulated in the depleted section. This results in lowering of the potential barrier for the injected electrons, which can enhance the overall photo-detection efficiency.
- The *photo-thermoelectric effect* is caused by the non-equilibrium distribution of photo-generated hot carriers in the graphene channel leading to a temperature gradient, ( $\Delta T$ ). This results in a photo-thermoelectric current expressed as

$$I_{\text{PTE}} = \frac{(S_1 - S_2)\Delta T}{R_{\text{DS}}}, \quad (2.7)$$

where  $S_{1/2}$  are the thermal coefficients of the two regions with different carrier densities. Based on the Mott relation, the coefficient in graphene can be expressed as [77]

$$S = -\frac{\pi^2 k_B^2 T}{2q} \frac{1}{\sigma} \frac{d\sigma}{dE_F}, \quad (2.8)$$

where  $k_B$  is the Boltzmann's constant,  $T$  is the temperature, and  $\sigma$  the electrical conductivity.  $E_F = \hbar\nu_F\sqrt{\pi n}$  is the Fermi energy of single layer graphene, with  $\hbar$  the reduced Planck constant, and  $\nu_F$  is the Fermi velocity.

- *Plasma-wave-assisted mechanism*. In 1993, M. Dyakonov and M. Shur [78] proposed a FET channel which could act as a cavity for plasma waves, and the generation of plasma waves by an external terahertz source. Consequently, terahertz detection could be realized by two different operations: i) a strong resonant photoresponse is predicted in the 2EDG channel when plasma damping rates lower than both the frequency of input signal and the inverse of the electron transit time; ii) a broadband terahertz response is observed when the plasma oscillations are overdamped. In the second case, the photoresponse can be calculated based on the diffusive transport model [79, 22]. The model predicts a second-order nonlinear response with the RF signal applied to the gate. This implies that the dc voltage response, is proportional to the derivative of the channel conductivity ( $\sigma$ ) with respect to the gate voltage, which can be expressed as,

$$\Delta U \propto \frac{1}{\sigma} \times \frac{d\sigma}{dV_G}. \quad (2.9)$$

In addition, the electric nonlinear model is widely used in GFET terahertz detection, which will be discussed in Chapter 3. The accurate modeling is very important to the development of GFET terahertz detection. This will require detailed investigation of GFET performance and characteristics, and accurate de-embedding of external circuit elements over a wide frequency range (or biasing range), which has been done in this thesis.





# Chapter 3

## GFET terahertz detector modelling and design

In this chapter, a model based on the electrical nonlinearity of GFETs will be analysed and discussed, and the second-order series expansion terms of the dc  $I - V$  will be presented. In addition, the design guidelines for detectors with better performance will be provided. Finally, the design and simulation of antennas will be presented, which is important for optimising the performance of antenna-integrated terahertz detectors.

### 3.1 Classical nonlinear electrical model for GFET detection

For power sensors, we can assume the RF signal is weak, hence the large signal model can be described with a Taylor expansion around the dc-bias point [41, 80]. Since the GFET has two control voltages, the small-signal drain-to-source current ( $i_{ds}$ ) is a function of the gate-source voltage ( $v_{gs}$ ) and the drain-source voltage ( $v_{ds}$ ) and can be expressed by the Taylor series as (limited to 2 orders)

$$i_{ds}(v_g, v_d) = g_{1,gs}v_g + g_{1,ds}v_d + \frac{1}{2}g_{2,gs}v_g^2 + \frac{1}{2}g_{2,ds}v_d^2 + g_{2,gs,ds}v_gv_d, \quad (3.1)$$

The coefficients of the Taylor series at the intrinsic bias point ( $V_{GSi}, V_{DSi}$ ) obtained from the derivatives of the drain-source current  $I_{DS}$  can be expressed as

$$g_{n,m} = \frac{\partial^n I_{DS}}{\partial V_{GSi}^n} |_{V_{DSi}}, \quad (3.2)$$

$$g_{n,ds} = \frac{\partial^n I_{DS}}{\partial V_{DSi}^n} |_{V_{GSi}}, \quad (3.3)$$

$$g_{2,gs,ds} = \frac{\partial^2 I_{DS}}{\partial V_{GSi} \partial V_{DSi}}. \quad (3.4)$$

Upon terahertz irradiation with a frequency of  $\omega$ ,

$$v_g = v_{THz} \cos(\omega t), \quad (3.5)$$

$$v_d = \alpha v_{THz} \cos(\omega t + \theta), \quad (3.6)$$

where  $\alpha$  is the amplitude ratio of  $v_d$  to  $v_g$  and  $\theta$  is the phase difference between them.  $v_{THz}$  is the input terahertz voltage which is determined by the antenna coupling and the

impedance matching between the GFET and the antenna. Thus, the dc current response generated by the even-order non-linearity can be expressed as

$$i_{\text{THz}} = \frac{1}{4}(g_{2,\text{gs}}v_g^2 + 2g_{2,\text{gs,ds}}v_gv_d \cos \theta + g_{2,\text{ds}}v_d^2), \quad (3.7)$$

Second-order Taylor series coefficients, i.e.,  $g_{2,\text{gs}}$ ,  $g_{2,\text{gs,ds}}$  and  $g_{2,\text{ds}}$ , are calculated from Equation (3.2-3.4) based on the measured dc  $I - V$  characteristics, as shown in Figure 3.1.

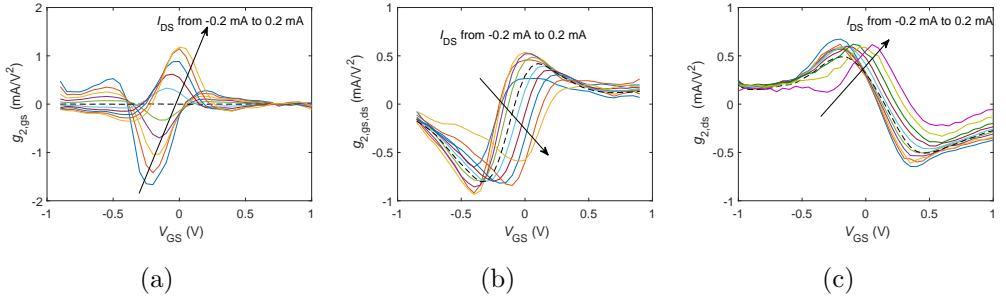


Figure 3.1:  $g_{2,\text{gs}}$  (a),  $g_{2,\text{gs,ds}}$  (b) and  $g_{2,\text{ds}}$  (c) of the detector in Paper A versus  $V_{\text{GS}}$  for different drain currents in the range from -0.2 to 0.2 mA with 40  $\mu\text{A}$  steps.

As shown in Figures 3.2 (a) and (b), there are two possible topologies of a GFET power detector:

- *With RF signal applied to the gate*,  $v_g$  is much larger than  $v_d$  as shown in Paper A, so the  $g_{2,\text{gs}}$  term in Equation 3.7 becomes the dominant part with the increase of the drain bias. When  $I_{\text{DS}}$  is zero, the  $\Re_V$  is not zero as  $g_{2,\text{gs}}$  due to the contribution of the  $g_{2,\text{gs,ds}}$  term.
- *With RF signal applied to the drain*,  $v_d$  is much larger than  $v_g$  [Paper A]. So the  $g_{2,\text{ds}}$  term in Equation 3.7 is the dominant part.

For the output voltage measured by a voltmeter, the detector can be modeled as a current source with an intrinsic source-drain resistance ( $r_{\text{ds}}$ ), as shown in Figure 3.3.

Thus the rectified voltage measured between the drain and the source terminals can be expressed as [81]

$$v_{\text{THz}} = \frac{i_{\text{THz}}r_{\text{ds}}R_{\text{M}}}{r_{\text{ds}} + R_{\text{D}} + R_{\text{S}} + R_{\text{M}}} \approx i_{\text{THz}}r_{\text{ds}}, \quad (3.8)$$

where  $R_{\text{M}}$  is the impedance of the voltmeter. The expression is simplified due to the relatively large value of  $R_{\text{M}}$ .

The voltage responsivity of the detector can be expressed as

$$\Re_V = \frac{v_{\text{THz}}}{P_{\text{ava}}(1 - |S_{ii}|^2)} \quad (3.9)$$

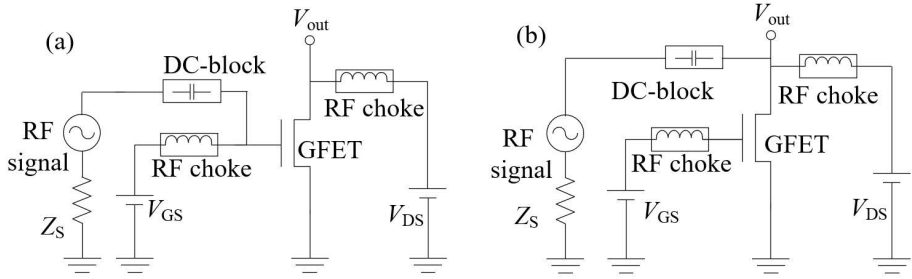


Figure 3.2: Topologies of a GFET detector with a RF signal applied to the gate (a) and the drain (b).

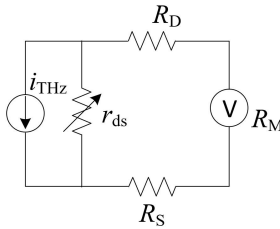


Figure 3.3: The equivalent readout circuit for a GFET detector.

where  $P_{\text{ava}}$  is the available input signal power to the detector, and  $S_{ii}$  is the complex reflection coefficient  $S_{11}$  or  $S_{22}$  depending on whether the input signal is applied to the gate or the drain. This is the maximum voltage responsivity that can be achieved by the power detector.

Finally, the  $g_2$  parameters extracted from the dc  $I - V$  characteristics can be used for modelling the voltage responsivity of detectors.

## 3.2 Design of GFET power detectors

According to above analysis, with the signal applied to the gate, the response depends on the  $g_{2,\text{gs}}$  and  $g_{2,\text{gs,ds}}$  terms in the drain-biased and unbiased- mode respectively; while with the signal applied to the drain, the response depends on the  $g_{\text{ds}2}$  term only. Therefore, the following approaches can be used to improve the performance of GFET power detectors:

- Increase the  $g_{2,\text{gs}}$ ,  $g_{2,\text{gs,ds}}$  and  $g_{2,\text{ds}}$  by reducing the residual carrier density experimentally demonstrated in Paper D.
- Increase the  $v_g$  and  $v_d$  by reducing the contact resistance and the gate capacitance.
- Apply the signal at both the gate and the drain ports with 180-degree relative phase difference.
- Increase  $g_{2,\text{gs}}$  by increasing the drain biasing with the signal applied to the gate.

- Design the size of the transistor, i.e. gate width ( $W$ ) and gate length ( $L$ ), to facilitate a reasonable impedance lever for RF circuit matching.

Note that both the contact resistance and the residual carrier density can be reduced via modifying the fabrication process [82]. And a lower gate capacitance can be achieved by reducing the gate length. The input impedance at the gate terminal and the drain terminal of the GFET in Paper A, were calculated from standard  $50\text{-}\Omega$  two-port S-parameters [41, 83], as shown in Figure 3.4. At 300 GHz, the real part of input impedance at the gate terminal is  $70\ \Omega$  which is used for the simulation of antennas in the next section.

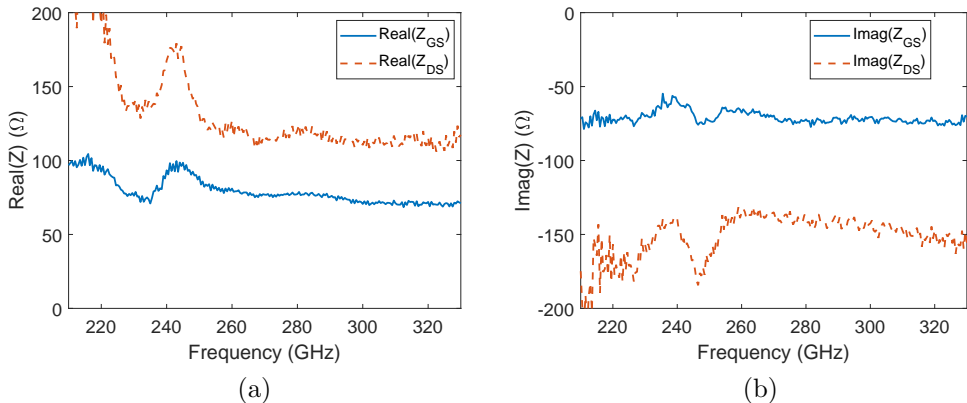


Figure 3.4: Real part (a) and imaginary part (b) of input impedance for the GFET in Paper A.

### 3.3 Design of planar antennas

For free-space radiation detection and imaging applications, the power detector is usually integrated with an antenna which can improve coupling efficiency between the antenna and the incoming radiation.

The input impedance and the directivity are two fundamental parameters of antennas. Figure 3.5 shows the simulated reflection coefficients of a bowtie antenna with radius of  $180\ \mu\text{m}$  and a dipole antenna with length of  $360\ \mu\text{m}$ . The centre working frequency of both the bow-tie antenna and the dipole antenna is around 300 GHz. The antenna bandwidth is often defined as the frequency range where the reflection coefficient ( $\Gamma$ ) is less than  $-10\ \text{dB}$ . The bandwidth of the bowtie antenna is around 100 GHz, which is approximately 2 times of that of the dipole antenna. The bowtie antenna were adopted in Paper D, F and G, because the bow-tie antenna has better bandwidth than conventional dipole and patch antennas.

Directivity of an antenna is the ratio of the radiation intensity in a given direction to isotropic radiation uniformly in all directions. Larger values of directivity imply a

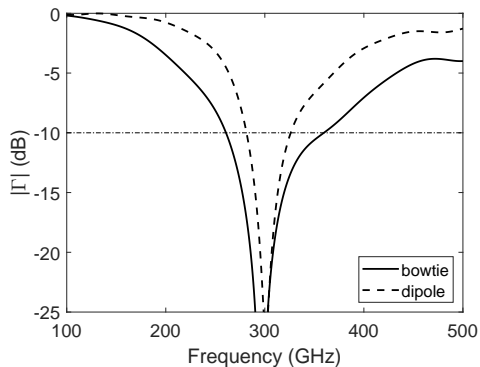


Figure 3.5: Reflection coefficients of bow-tie and dipole antennas simulated by using CST with an input impedance of  $70 \Omega$ .

more focused antenna. Maximising the directivity will couple more terahertz radiation into detectors, hence improve the detection performance. The simulated directivity of a bow-tie antenna with radius of  $150 \mu\text{m}$  at 300 GHz is shown in Figure 3.6. The maximum directivity of single bow-tie antenna is 3 dB, as shown in Figure 3.6 (b). To increasing the  $H$ -plane directivity, two parallel metal strip arrays can be placed beside the antenna [84], as shown in Figure 3.6 (c). The antenna with optimised directivity is used for the linear array in Paper G. The maximum directivity increases from 3 dB to 6 dB, as shown in Figure 3.6 (d).

Furthermore, an efficient method of increasing directivity is using dielectric lenses or horn antennas. The simulated directivity of a bow-tie antenna attach on a hyperhemispherical silicon lens with a radius of 5 mm and an extension thickness of 1.5 mm at 487 GHz is shown in 3.7.

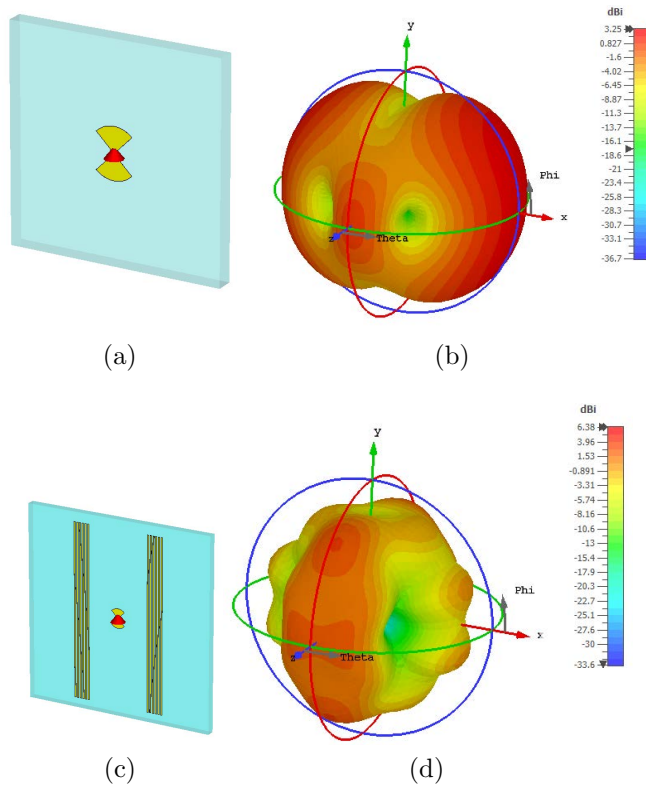


Figure 3.6: Directivity. (a) Layout (a) and the corresponding directivity (b) of a bow-tie antenna. Layout (c) and the corresponding directivity (d) of a bow-tie antenna coupled with parallel metal strip arrays. (simulated by using CST).

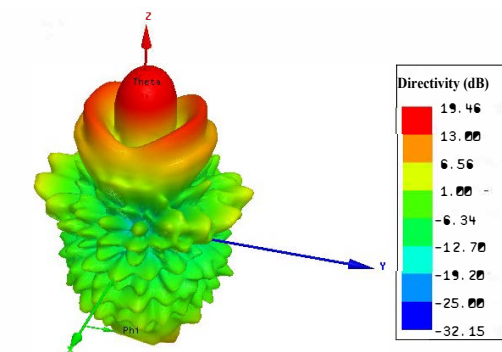


Figure 3.7: Directivity of a bow-tie antenna coupled with a Si lens (simulated by HFSS).

# Chapter 4

## Fabrication of GFET detectors

For high-performance detectors, state-of-the-art fabrication processes are required. In this chapter, a new fabrication process for GFET detectors on rigid and flexible substrates is introduced. Moreover, the fabrication techniques with emphasis on properties of three critical interfaces are discussed. These interfaces include the interface between graphene and the substrate, the interface between graphene and the metal (ohmic contact), and the interface between graphene and the gate dielectric.

### 4.1 Fabrication process flow of GFET detectors

In contrast with silicon technology, current manufacturing processes of graphene devices still needs improvement. Graphene devices have a strong performance variation depending on the fabrication techniques. In particular, surface contaminations during the fabrication process lead to formation of the charged impurities resulting in reduced carrier mobility and higher residual concentration of the charge carriers, which can largely degrade device performance and reliability [85].

Figure 4.1 shows the fabrication process flow of GFET detectors optimised with the aim of achieving graphene with low-resistance ohmic contacts and low residual carrier concentration, which is required for high-performance detectors. The graphene was first covered with a  $\text{Al}_2\text{O}_3$  layer to reduce contaminations during following processing steps. This step sets it apart from the previously used fabrication process [21], and results in a cleaner gate dielectric/graphene interface and, hence, a lower residual carrier density. Furthermore, the fabrication of the gate dielectric, electrodes and pad contact are combined into one step, which also improves the device performance. The details of processing steps shown in Figure 4.1, are listed below.

- *Graphene on substrate.* The graphene in this work was grown by CVD on copper foils and transferred onto  $\text{Si}/\text{SiO}_2$  or plastic substrates.
- *Protective layer.* The protective layer was deposited by repeating a sequence of depositing 1 nm Al layers and natural oxidizing in air 4 times. The van der Waals gap between Al and graphene allows oxygen molecules to penetrate deep into the interface and form a high-quality oxide [86].
- *Mesa isolation.* The graphene mesa were defined by e-beam lithography. The  $\text{Al}_2\text{O}_3$  and the graphene outside the mesa were removed by buffered oxide etchant (BOE) and oxygen plasma, respectively.

- *Ohmic contact.* The source and drain electrodes were patterned by a sequence of e-beam lithography,  $\text{Al}_2\text{O}_3$  etching, Ti/Pd/Au deposition, and lift-off.
- *Gate dielectric and gate electrode.* After patterning of the gate area by e-beam lithography, the gate dielectric was deposited by repeating a sequence of depositing 1 nm Al layers and natural oxidizing 6 times. Al/Au gate electrodes were then formed by using standard deposition and lift-off technology.

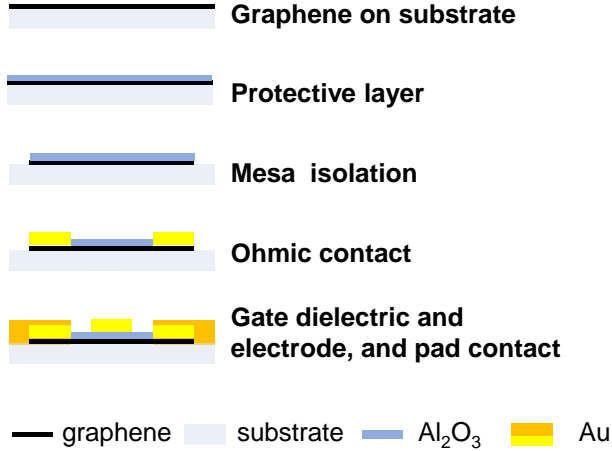


Figure 4.1: Schematics of the fabrication processes optimised for high performance GFET detectors.

The detailed process parameters for Paper A and F are listed in Appendix A and B, respectively.

## 4.2 Graphene growth and transfer

There are three major approaches to obtain high-quality graphene sheets: the scotch tape method [34], epitaxial growth on SiC substrates [87], and CVD on metal foils [88]. For commercial viability, low-cost and scalable large-area synthesis is necessary. Thus, mechanical exfoliation using adhesive tapes is clearly not an option. The CVD graphene can be transferred onto any substrate and integrated into standard complementary metal-oxide-semiconductor (CMOS) processes, this being a promising candidate for FETs on bendable substrates. Moreover, CVD growth of graphene may fix issues of cost and scalability for future commercial flexible circuits and integrated systems. In 2016, X. Xu has demonstrated an ultrafast growth method of single-crystal graphene with a growth rate of  $60 \mu\text{m/s}$  [89]. Consequent to growing graphene on copper foils, there has to be a reliable method for transferring graphene onto substrates. In 2007, Smith et al. have statistically evaluated the yield of GFETs on a wafer scale, which reveals that device



failure occurs primarily during the graphene transfer step [90]. CVD graphene transfer methods can be categorized into dry transfer [91] and wet transfer [92, 93].

In this work, the graphene provided from Graphenea was CVD-grown on copper foils and wet transferred onto Si/SiO<sub>2</sub> [Paper A and Paper D], polyethylene terephthalate (PET) [Paper E and Paper F ], and polyethylene naphthalate (PEN) [Paper G] substrates.

### 4.3 Substrates

The material properties of commonly used substrates for GFETs are listed in Table 4.1, and vary greatly from material to material. The PET and PEN sheets were chosen as the

Table 4.1: Material properties of commonly used substrates for GFETs [94, 95, 96].

Property	PEN	PET	PI	PDMS	Si
Young's modulus (MPa)	620	$\sim 3 \times 10^3$	$4 \times 10^3$	0.36-0.87	$1.3-1.8 \times 10^5$ [97]
Density (g/cm <sup>3</sup> )	1.36	1.38	1.42	0.976	2.329
Relative permittivity ( $\epsilon_r$ )	3.2-3.4	2.9	$\sim 3.5$	2.3-2.8	11.9
Glass transition temperature ( $T_{gl}$ ) (°C)	128	81	300-410	N/A	N/A
Thermal conductivity (W/mK)	0.15	$\sim 0.2$	$\sim 1$	0.15	156
Electrical resistivity ( $\Omega\text{cm}$ )	$1 \times 10^{15}$	$1 \times 10^{17}$	$1.5 \times 10^{17}$	$4 \times 10^{13}$	$1 \times 10^4$

flexible substrates in Paper F and G respectively for with the following reasons:

- *Mechanical property.* PET and PEN with high Young's modulus can tolerate a high level of strain.
- *Chemical compatibility.* PET and PEN are insoluble in chemicals used during the device fabrication, such as BOE and organic solvents for the development of e-beam and photo-resists, which is a necessary property for use as a substrate in electronics.
- *Low loss tangent.* Substrates with low loss tangents are required for the high-frequency applications.

However, unlike the normal rigid substrates, e.g. Si, GaN, and glass, there are several limitations affecting the fabrication of devices on PET and PEN:

- *Relatively high surface roughness.* The theoretical model of van der Waals interaction [98] predicts that the surface roughness of the substrate can affect the adhesion of the graphene layers. The study of Ishigami et al has shown that graphene carrier mobility is limited by scattering caused by substrate surface roughness [99]. SiO<sub>2</sub>/Si interface roughness plays an important role in the mobility fluctuation noise in MOSFETs [100]. To understand and characterise the interfacial adhesion of graphene on substrates, it is essential to characterise the surface roughness. As

shown in Figure 4.2, the surface roughness of the PET is considerably greater than that of the Si/SiO<sub>2</sub> (300 μm/300 nm) substrate. Thus, the adhesion of graphene on PET is potentially less than that on Si/SiO<sub>2</sub>, which requires development of more gentle fabrication processes to avoid graphene detachment. Moreover, the highly uneven surface topography of plastic substrates limits the fine resolution of lithography.

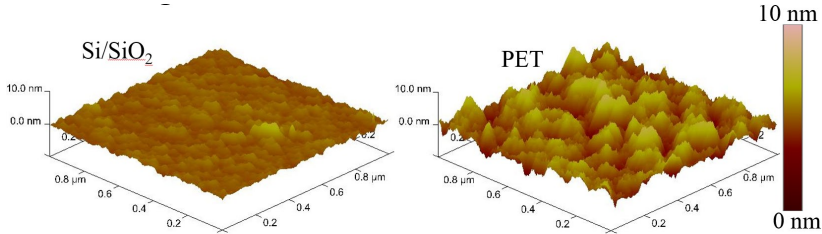


Figure 4.2: Atomic force microscope (AFM) images of Si/SiO<sub>2</sub> substrate (left), and PET substrate (right).

- *Low processing temperature.* During exposure to high temperature processes, even below the glass transition temperatures ( $T_{gl}$ ), the sample is subjected to build-in stress, which has to be minimised. The glass transition temperatures for crystalline PET and PEN are 81 °C [95] and 128 °C [101], respectively. Thermally induced crystallization occurs when the plastic is heated to above  $T_{gl}$ . If the processing temperature is higher than  $T_{gl}$ , the mismatch in thermal expansion coefficients between plastic substrates and resists may induce non-negligible film curvatures. Additionally, it is impossible to decrease the fixed charge density and interface state density of graphene on plastic substrates by annealing at temperatures as can be done with silicon substrates.
- *Electron radiation Damage.* For insulating substrates, charges occurring during electron-beam lithography (EBL) cannot be appropriately discharged from the substrates and may distort the structures, as shown in Figure 4.3. This problem can be eliminated if a conductive layer is applied on the e-beam resist prior to EBL.

## 4.4 Ohmic contact

To minimise the parasitic resistances in graphene devices, highly conductive ohmic contacts are necessary [102]. Ohmic resistance can be reduced by using metal with large work function [103]. In this thesis, palladium (Pd) with work function of around 5.5 eV is selected for the ohmic contact. Furthermore, metals in contact with monolayer graphene can shift the Fermi level below the electrodes in graphene. This results in the formation of an interface dipole layer due to charge transfer because of the low density of states in graphene. A consequence of this interface dipole formation is the typically observed asymmetry between the hole and electron contact resistance in graphene devices.

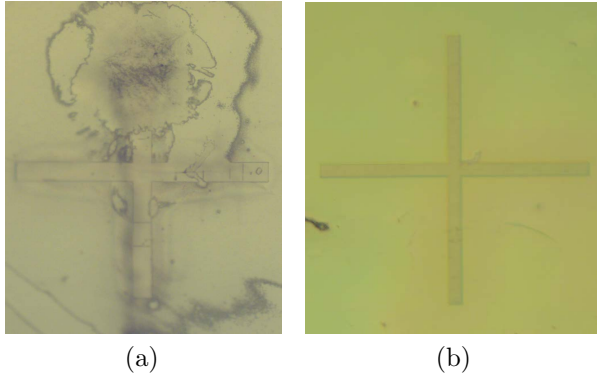


Figure 4.3: Optical micrographs of a cross mark on PET substrate after develop without (a) and with (b) a conductive layer.

## 4.5 Gate dielectric

To ensure the high performance of terahertz detectors and to reduce leakage current, a uniform and manufacturable gate dielectric film with good electrical properties is needed [104, 105]. The  $\text{SiO}_2$  and the high- $\kappa$  dielectrics (e.g.  $\text{Al}_2\text{O}_3$ ,  $\text{HfO}_2$ ,  $\text{TiO}_2$ , and  $\text{ZrO}_2$ ) developed for conventional rigid electronics generally reveal impressive electronic performance. However, these dielectric materials can only be used in applications that require modest flexibility. If large stretchability is necessary, polymeric dielectrics such as polydimethylsiloxane (PDMS) [106], polymethyl methacrylate (PMMA) [107] or polyimide (PI) [108] obtained by spin coating, casting or printing at room temperature, are generally used. In addition, hybrid dielectrics that include both high- $\kappa$  oxides and polymers have been demonstrated with excellent mechanical flexibility, large dielectric constant, and low leakage current [109].

Defect-free graphene is hydrophobic and inert, and there are no dangling bonds on its surface. Thus, it is difficult to directly deposit polar thin film gate dielectrics (e.g.  $\text{Al}_2\text{O}_3$ ,  $\text{HfO}_2$  and  $\text{SiO}_2$ ) on graphene. To solve this problem, a thin inert buffer layer or seed layer followed by atomic layer deposition (ALD) of the main dielectric film [110, 111] is widely used. However, the properties of the gate dielectric film on graphene are very sensitive to the growth conditions. Thus, techniques to characterise the electrical properties of the dielectric film on graphene are very important.

In Paper E, the fabrication and characterisation of parallel-plate capacitor test structures to evaluate the electrical properties of the dielectric film are presented. The test structure consists of a metal/dielectric/graphene stack on a PET substrate and requires only one lithography step for the patterning of the topside metal electrodes. The leakage current is less than  $100 \mu\text{A}/\text{cm}^2$  when the gate voltage is 5 V, which is negligible compared to drain current in GFETs and photocurrent in GFET terahertz detectors [22]. The breakdown electric field is about 5 mV/cm, which is similar to reported  $\text{Al}_2\text{O}_3$  ALD films on silicon [112]. The dielectric constant calculated from the measured capacitance

is approximately 7.6, which is comparable with that of the bulk material. In addition, the results and analysis in Paper E indicate that the measured loss tangent is governed mainly by the dielectric loss in  $\text{Al}_2\text{O}_3$  and can be associated with charged defects.

# Chapter 5

## On-wafer characterisation of GFET detectors

Accurate characterisation of terahertz power detectors is a challenging task. This is because the high-frequency response is mainly dominated by parasitic coupling and loss associated with contacts, substrates, and overall layout of the component. In this chapter, the accurate and comprehensive terahertz on-wafer probe characterisation will be presented. The method provides accurate calibration of power in close vicinity of the device under test, and allows simultaneously measurements of the dc  $I - V$  characteristics, the S-parameters, and the GFET detector response from 1 GHz to 1.1 THz. Moreover, the on-wafer probe characterisation of IF bandwidth and low-frequency noise will be included.

### 5.1 DC characterisation

An accurate dc characterisation is essential for modelling, design and fabrication of GFET detectors. The dc transfer curves of GFETs can be used for the evaluation of residual carrier concentration, mobility and contact resistance, which are basic device parameters. Furthermore, based on the nonlinear electrical model,  $g_2$  parameters, calculated from dc  $I - V$  characteristics, is necessary for predicting RF detection performance of GFETs.

Figure 5.1 shows a schematic block diagram of a dc characterisation setup for GFETs. Sourcemeters can provide precision voltage and current sourcing as well as measurement capabilities.

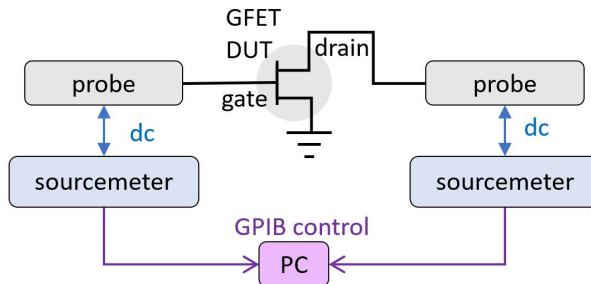


Figure 5.1: A schematic block diagram of a dc characterisation setup.

Figure 5.2 (a) shows the experimental  $V_{DS}(V_{GS}, I_{DS})$  of the GFET in [Paper A]. The

dashed lines indicate the values of  $V_{\text{Dir}}$  with different bias. The field-effect mobility ( $\mu$ ), the residual carrier concentration ( $n_0$ ), and the sum of parasitic source and drain resistances, can be extracted by fitting the measured source-drain resistance ( $R_{\text{DS}}$ ) to the drain resistance model [111, 113]:

$$R_{\text{DS}} = R_S + R_D + \frac{L}{Wq\mu\sqrt{n_0^2 + n_G^2}}, \quad (5.1)$$

where  $L$  and  $W$  are the gate length and width, respectively; and  $q$  is the electron charge.  $n_G$  is the carrier density induced by the gate voltage, which can be obtained from the following equation relating the gate capacitance per unit area and the quantum capacitance of graphene:

$$V_{\text{GS}} - V_{\text{Dir}} = \frac{qn_G}{C_G} + \frac{\hbar v_F \sqrt{\pi n_G}}{q}, \quad (5.2)$$

where  $V_{\text{Dir}}$  is the gate voltage of the Dirac point,  $C_G$  is the gate capacitance per unit area,  $v_F$  is the Fermi velocity of graphene, and  $\hbar$  is the Planck's constant. Note that the model is a semi-empirical model with the assumption that graphene transport properties are dominated by Coulomb scattering [114] and, hence mobility does not depend on the concentration of charge carriers [85]. Figure 5.2 (b) shows the measured and modelled drain-source resistance,  $R_{\text{DS}} = V_{\text{DS}}/I_{\text{DS}}$ , of the GFET detector in [Paper A] as a function of  $V_{\text{GS}}$  at  $I_{\text{DS}} = 10 \mu\text{A}$ . The asymmetric conductance curves are due to the additional resistance produced by the p-n junctions between the n-type gated channel and the p-type ungated regions at positive values of  $V_{\text{GS}}$ . The extracted parameters are listed in Table 5.1.

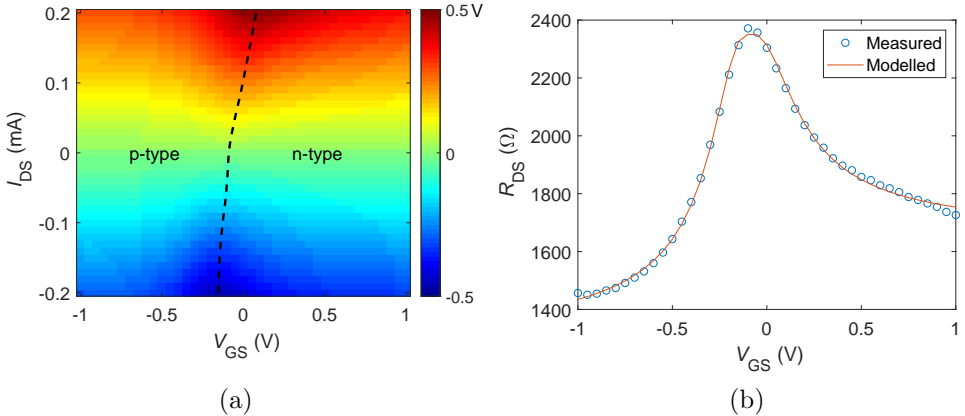


Figure 5.2: (a) 2D color plots of the experimental  $V_{\text{DS}}$  of the GFET in [Paper A] as a function of  $I_{\text{DS}}$  and  $V_{\text{GS}}$ . (b) The experimental and modelled drain-source resistance of the GFET detector in [Paper A] as a function of  $V_{\text{GS}}$ .

Table 5.1: Extracted parameters of the detector in [Paper A].

$n_0$ ( $10^{11}$ $\text{cm}^{-2}$ )	$\mu_e$ ( $\text{cm}^2/\text{Vs}$ )	$\mu_h$ ( $\text{cm}^2/\text{Vs}$ )	$R_{S,e} + R_{D,e}$ ( $\Omega$ )	$R_{S,h} + R_{D,h}$ ( $\Omega$ )
4	4000	5000	1300	1600

## 5.2 Scattering parameter characterisation

Using the equivalent circuit in Figure 2.3, the values of the equivalent circuit elements can be derived from measured S-parameters through fitting techniques [64]. For accurate characterisation of power detectors, it is necessary to know the power loss and the reflected energy. Overall, S-parameter characterisation is very important to analysis of high-frequency GFET detection. With the advancements in terahertz ground-signal-ground (GSG) probes [115], on-wafer S-parameter measurements have been progressively extended from the microwave to the terahertz frequency range.

Figure 5.3 shows the terahertz on-wafer S-parameter measurement setup. The signal provided by a vector network analyzer (VNA) with extender modules is applied to the gate or drain using GSG probes. RF and dc signals are separated by an bias-tee. S-parameters are measured by the network analyzer under different gate and drain bias conditions.

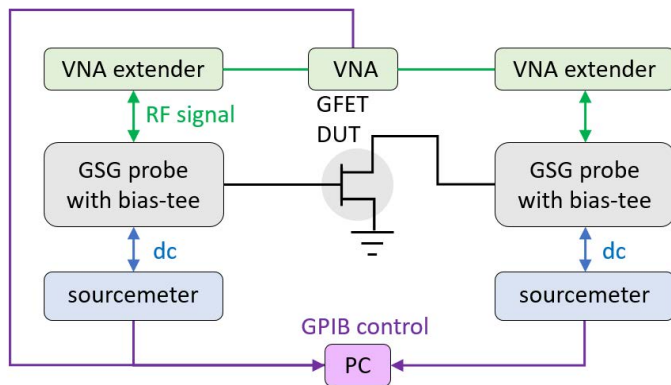


Figure 5.3: A schematic block diagram of a S-parameter characterisation setup.

For actual transistor two-port parameters from the measurement setup, two important correction procedures have to be followed:

1. *Setup calibration* by defining a reference plane for the S-parameter measurements at the probe tips using a standard 2-port on-wafer calibration technique. For lower frequencies, a short-open-load-thru (SOLT) procedure is commonly used, and the calibration kits are often provided by commercial companies. For higher frequency ranges, the on-wafer calibration is often performed with thru-reflect-line (TRL) calibration kits that should preferably be designed and fabricated on the same substrate as the devices under test [116, 117]. TRL calibration kits consist of three

kinds of standards, i.e., through, short and  $\lambda/4$  line.

2. *On-wafer parasitics characterisation.* The parasitic capacitances and inductances can be extracted from measured S-parameters using open and short de-embedding structures, respectively [65].

Figure 5.4 shows the measured and modeled S-parameters of the GFET in [Paper A] at  $V_{GS} - V_{Dir} = -0.2$  V and  $I_{DS} = 0$  A in the frequency range of 1 GHz to 67 GHz. The circuit elements were extracted from the measured GFET two-port S-parameters [118], and are shown in table 5.2.

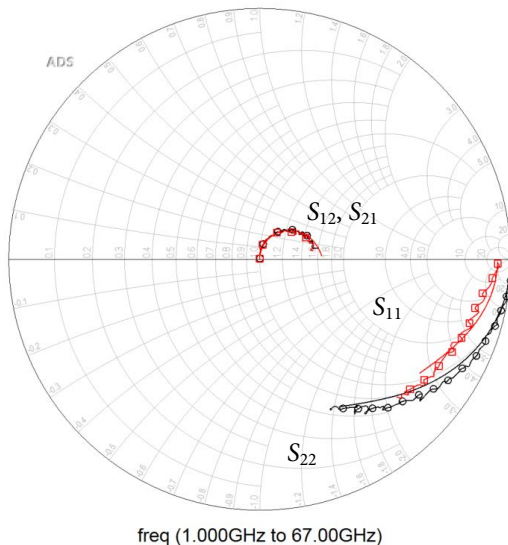


Figure 5.4: Experimental and simulated S-parameters of the detector in [Paper A].

Table 5.2: Extracted parameters of the GFET in [Paper A]

$L$ ( $\mu\text{m}$ )	$W$ ( $\mu\text{m}$ )	$C_{gs}$ (fF)	$C_{gd}$ (fF)	$C_{DS}$ (fF)	$R_{S/D}$ ( $\Omega$ )	$r_i$ ( $\Omega$ )	$r_{ds}$ ( $\Omega$ )
1.2	5	9	9	1	300	1	1400

### 5.3 RF power detector characterisation

With strong effects of parasitic coupling and losses at high frequencies, accurate characterisation of terahertz power detectors is a challenging task. For accurate power detector characterisation and for reducing the uncertainty from the setup and devices, it is important to carry out simultaneous measurements of the dc  $I - V$  dependence, the S-parameters, and the detection performance.



Figure 5.5 shows a terahertz on-wafer probe direct detection setup for simultaneous measurements of dc  $I - V$  dependence, S-parameters, and GFET detector response over a wide frequency range. The dc voltage and current are provided and measured by two sourcemeters. The S-parameters are measured using a VNA and extender modules. The rectified response between drain and source is measured using a lock-in amplifier.

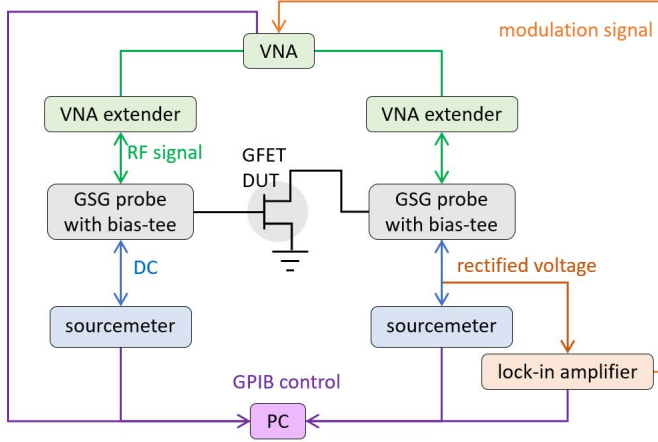


Figure 5.5: A schematic block diagram of the on-wafer RF detection setup.

Figure 5.6 (a) show the  $\mathfrak{R}_V$  versus frequency from 1 GHz to 1.1 THz with the signal applied to the gate and the drain, respectively. The  $\mathfrak{R}_V$  shows  $1/f^2$  dependence at higher frequencies in agreement with the simulation results. Note that the  $\mathfrak{R}_V$  increases at lower frequencies with the signal applied to the gate because high-impedance mismatch at lower frequencies may reduce the accuracy of the characterisation. The dash-dot lines indicate that cut-off frequencies are around 140 GHz and 50 GHz with the signal applied to the gate and the drain, respectively. Figure 5.6 (b) shows that the measured voltage response at the given  $V_{GS} = 0$  V is linear with the incident power of the RF signal. The incident power drives the detector into saturation.

Figure 5.7 (a) and (b) shows the voltage responsivity versus bias of the device with a 300 GHz signal applied to the gate and drain, respectively. With the RF signal applied to the gate, the  $\mathfrak{R}_V$ , at  $V_{GS}$  close to the Dirac point ( $V_{Dir}$ ), is proportional to  $I_{DS}$ , which follows the same trend as the  $g_{2,gs}$  in Figure 3.1 (a) except that under cold condition. When  $I_{DS}$  is zero, the  $\mathfrak{R}_V$  is not at zero as  $g_{2,gs}$ , due to the contribution of the  $g_{2,gs,ds}$  term. With the RF signal applied to the drain, the sign of the  $\mathfrak{R}_V$  changes from positive to negative with increasing  $V_{GS}$ . As  $I_{DS}$  increases, there is a positive shift of the  $\mathfrak{R}_V$  curves with no obvious changes of the maximum of  $\mathfrak{R}_V$ , which follows the trend of the  $g_{2,ds}$  exactly. There is a good agreement between experimental and simulation data.

Figure 5.8 (a) and (b) show the maximum absolute values of the experimental and simulation  $\mathfrak{R}_V$  versus  $I_{DS}$  with 300 GHz signals applied to the gate and drain, respectively. With the RF signal applied to the gate, For negative biasing, the maximum value of the  $\mathfrak{R}_V$  increases up to 1.8 kV/W with  $I_{DS} = -0.2$  mA. With the RF signal applied to the

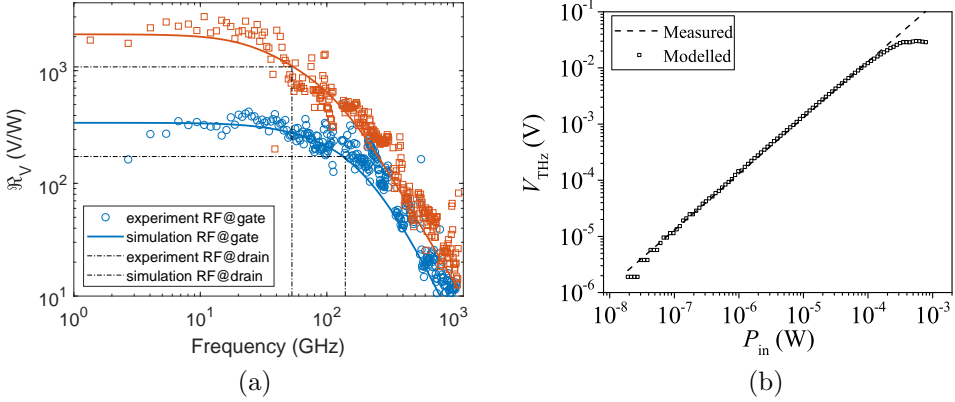


Figure 5.6: (a) Experimental and simulated voltage responsivity of the detector in [Paper A] versus frequency. (b) Measured voltage response (black solid squares) of a detector at 1 GHz as a function of the input power. The black square symbols are the experimental data and the dashed line shows the ideal square law response.

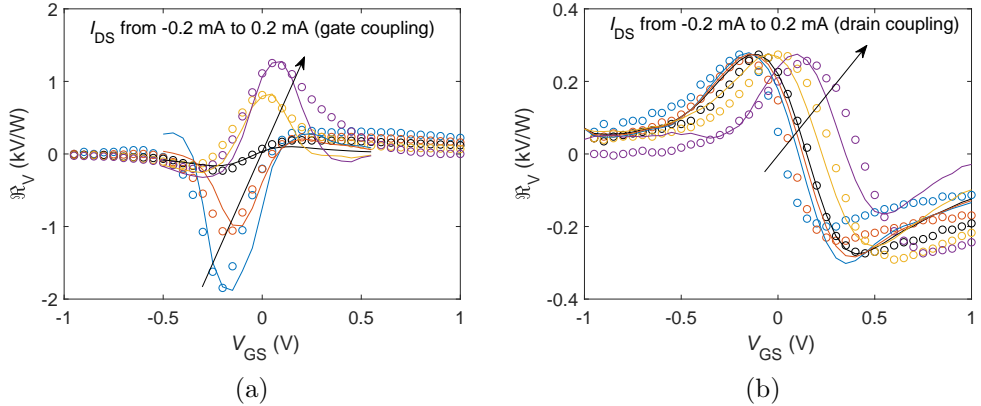


Figure 5.7: Experimental (symbols) and simulated (solid lines) maximum  $|\Re_V|$  of the detector in [Paper A] versus  $V_{\text{GS}}$  with a 300 GHz signal applied to the gate (a) and drain (b).

drain, the maximum of  $\Re_V$  is approximately 300 V/W. More detailed analysis of biasing and frequency dependencies of responsivity is shown in [Paper A].

Overall, the on-wafer characterisation results indicate that the broadband terahertz response of GFET detectors can be fully described using a combination of a quasi-static equivalent circuit model, and the second-order series expansion terms of the nonlinear dc  $I - V$  characteristic.

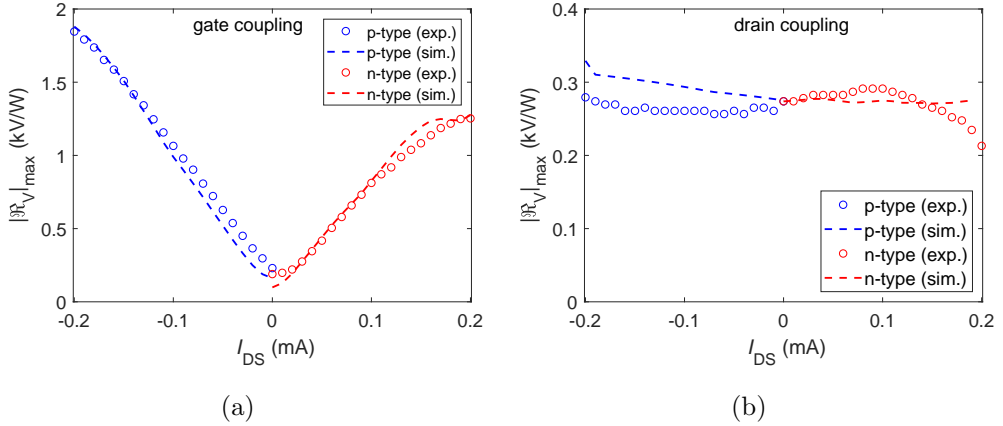


Figure 5.8: Experimental (symbols) and simulated (solid lines) maximum  $|\mathfrak{R}_V|$  of the detector in [Paper A] versus  $I_{DS}$  with a 300 GHz signal applied to the gate (a) and drain (b).

## 5.4 IF bandwidth characterisation

The GFETs have shown the potential for high-sensitive and high-speed terahertz detectors at room temperature. Qin et al. [29] and Generalov et al. [119] have demonstrated GFETs detectors with IF bandwidths of 1 GHz and 5 GHz in quasi-optical setups, respectively. However, these results can be limited by the readout circuits and instruments. The IF bandwidth of GFETs can be characterized using the experimental setup shown in Figure 5.9. The LO and RF signals provided by extenders are fed to the mixers by GSG probes. The dc gate bias is provided by a sourcemeter. The IF signals is measured using infinity probes and a spectrum analyzer.

Figure 5.10 (a) shows the block diagram of the GFET heterodyne detector circuit in Paper B. Coupled line high-pass filters are implemented at both the LO and RF ports. The low-pass filter at the IF port consists of a quarter wavelength open stub and stepped-impedance lines. The dc pass-filter is implemented by a high-impedance transmission line. Full-wave EM simulations using CST microwave studio were applied for optimizing layout dimensions.

Figure 5.10 (b) shows the normalized conversion efficiency of GFET heterodyne detectors versus the IF frequency. The 3-dB IF bandwidth ( $f_{3dB}$ ), extracted by fitting the measured CE with  $CE = CE_0 - 20\log(f_{IF}/f_{3dB})^2$ , was found to be around 56 GHz for the GFET with the gate length of  $0.6 \mu\text{m}$ . The results demonstrate the switching speed of GFETs detectors, which is important for future applications. Note that conversion loss (CL) is estimated to be 28 dB at local oscillator power of 13 dBm, which could reduce to 21 dB assuming 2 times lower contact resistance. To compete with other technologies, further optimisations are needed.

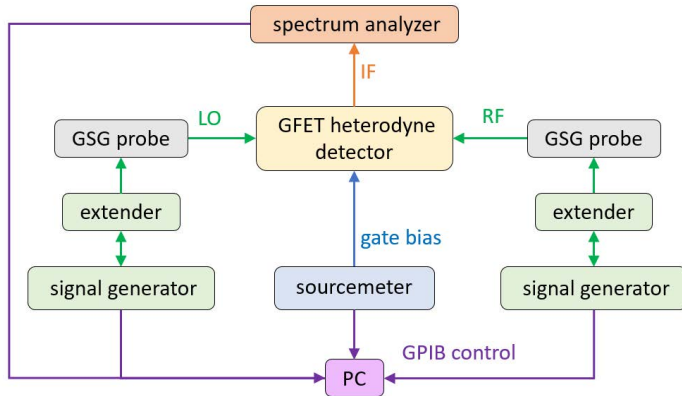


Figure 5.9: A schematic block diagram of the on-wafer probe characterisation of IF bandwidth.

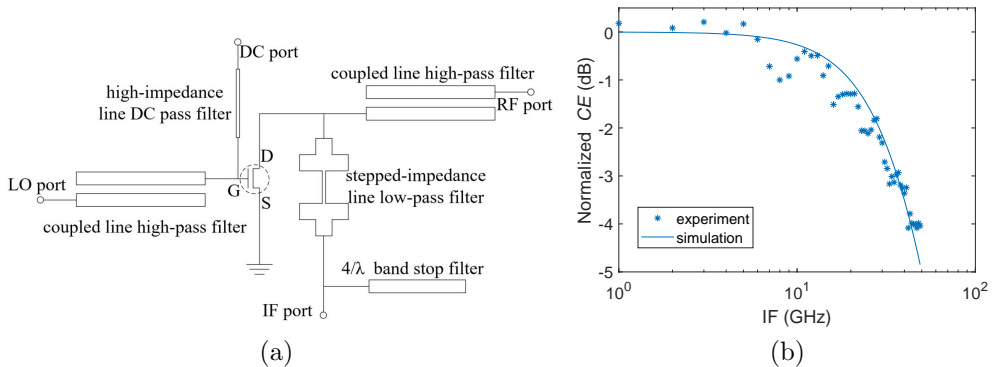


Figure 5.10: Block diagram (a) and normalized conversion efficiency versus IF frequency at an LO frequency of 220 GHz (b) of the mixer circuit in Paper B.

## 5.5 Low-frequency noise characterisation

As an important figure of merit of direct power detectors, the NEP is often estimated based on the voltage responsivity and the thermal noise. However, for GFET detectors, impurities and other defects introduced during the fabrication process can contribute to the low-frequency noise [120], which may degrade the detector noise performance. In Paper C, the low-frequency noise in GFET terahertz detectors has been characterized. This facilitates finding a low frequency limit of the modulation frequency, above which the low-frequency noise is negligible. The low-frequency noise spectral density can be measured using a low-frequency noise analyzer, as shown in Figure 5.11. The noise from the device is amplified and analyzed using a high-speed digitizer. The SMUs with low

pass filters are used to apply bias and measure dc  $I - V$  characteristics.

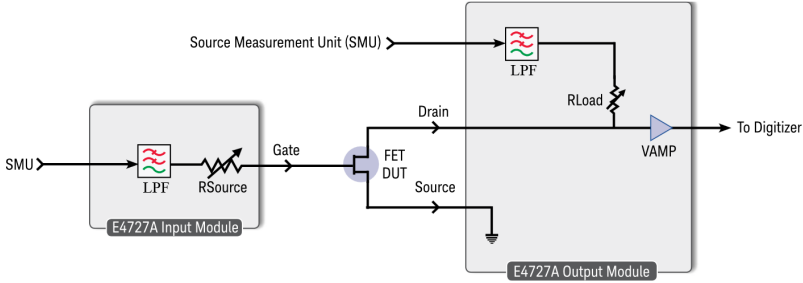


Figure 5.11: Low-frequency noise measurement topology [Keysight E4727A Advanced Low-Frequency Noise Analyzer Data Sheet].

Figure 5.13 shows the low-frequency noise spectral density of the GFET detector in [Paper A], which reveals a  $1/f$  spectral dependence. The  $1/f$  noise is caused by fluctuations in concentration and/or mobility of carriers in the channel [120], which follow the Hooge model expressed as the Equation (2.5).

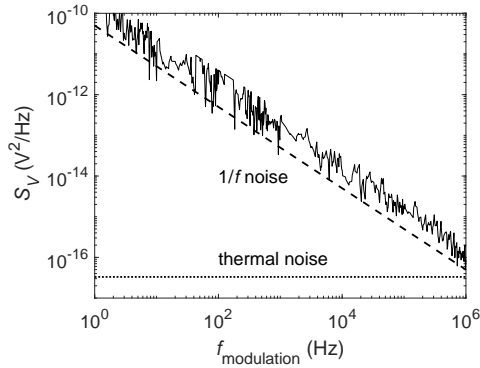
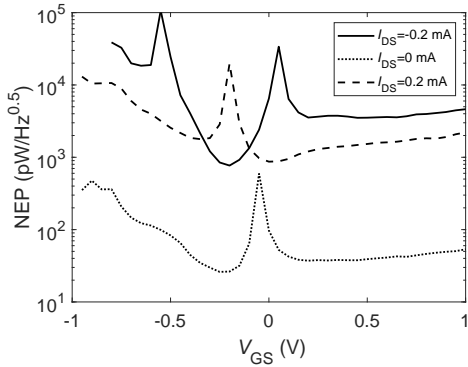
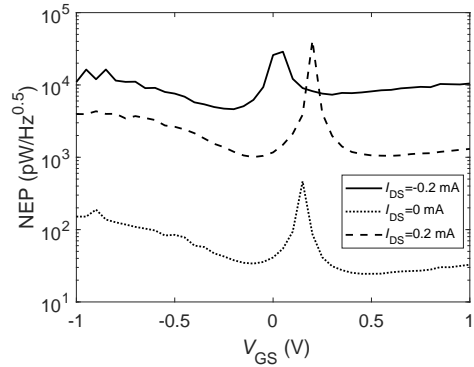


Figure 5.12: Measured noise spectral density of the GFET in [Paper A].

Figures 5.13 (a) and (b) show the estimated NEP as a function of  $I_{DS}$  at the modulation frequency of 1 kHz with a 300 GHz signal applied to the gate and the drain, respectively. At low modulation frequencies, the NEP increases with the drain biasing, since  $1/f$  noise is the main noise of the detector. While at high modulation frequencies NEP decreases with the current biasing when the THz signal is applied to the gate, which is due to the increase of responsivity with the drain bias. At 1 kHz modulation frequency, the minimum NEP of 26 and 24  $\text{pW}/\sqrt{\text{Hz}}$  with 300 GHz signal applied to the gate and the drain respectively, appears at zero drain biasing. The low-frequency noise measurements indicate the minimum modulation frequency dominated by the thermal noise, which sets the necessary switching time to reduce the effect of  $1/f$  noise.



(a) *gate coupling*



(b) *drain coupling*

Figure 5.13: Estimated NEP versus  $V_{GS}$  of the GFET detector in [Paper A] with a 300 GHz signal applied to the gate (a) and the drain (b).

# Chapter 6

## Antenna-integrated GFET terahertz detectors

This chapter will present the characterisation of antenna-integrated GFET terahertz detectors including detectors on rigid substrates [Paper D], detectors on flexible substrates [Paper F] and detector arrays on flexible substrates [Paper G]. In addition, effects of the graphene quality, the bending strain and the antenna directivity on the performance of GFET detectors are highlighted.

### 6.1 Free-space terahertz detection setup

Antenna-integrated detectors and detector arrays are widely used in free-space sensing and imaging. Terahertz integrated antennas are usually physically small and have a small effective aperture for receiving the incoming radiation. Therefore, they are often placed at the focal plane of antennas, lenses or mirrors to increase detection performance. The commonly used quasi-optical components with very high coupling efficiency include horn antennas, hyper-hemispherical high-resistivity silicon lenses, plastic plano-convex lenses and off-axis parabolic mirrors.

Figure 6.1 shows a schematic image of a free-space terahertz detection setup. The terahertz signal is transmitted by a horn antenna mounted on the waveguide flange of the extender, focused onto the sample under test by two plastic plano-convex lenses. In order to reduce the effect of  $1/f$  noise, the rectified detector voltage signal between the drain and the source is commonly measured using a lock-in amplifier that provides a modulation frequency to a terahertz transmitter or a chopper. Note that different publications usually use different setups with different losses and different power calibration tools and procedures. Therefore, it is difficult to compare detector performance in different publications.

### 6.2 GFET detector

Detectors based on antenna-integrated GFETs have shown their potential for wide-band, high-speed and high-sensitivity room-temperature terahertz detection [22, 29]. However, graphene devices have a strong performance variation depending on the fabrication techniques [85]. By means of modifying the previous fabrication process [21], a high-performance 400-GHz GFET detector on a Si/SiO<sub>2</sub> substrate has been demonstrated in [Paper D]. The detector is based on a GFET integrated with a bow-tie antenna that

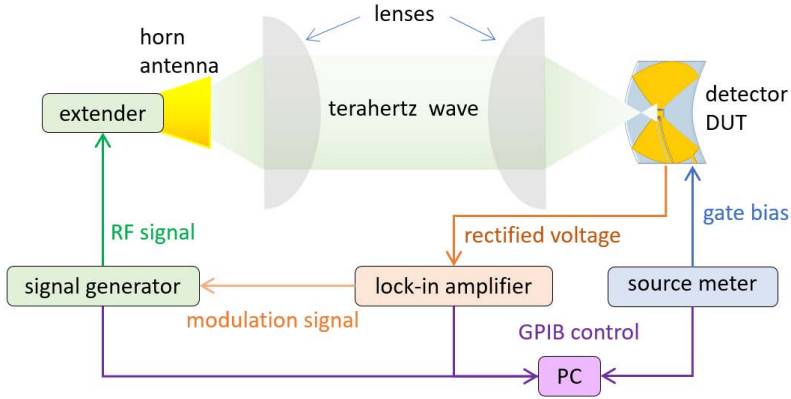


Figure 6.1: A schematic image of a free-space measurement setup of antenna-integrated detectors.

provides an asymmetric coupling condition between the source and the drain, as shown in Figure 6.2 (a).

The experimental and simulated voltage responsivity as a function of the gate voltage is shown in Figure 6.2 (b). The solid line represents the simulated results based on the electrical nonlinear model described in Chapter 3. The estimated maximum voltage responsivity and corresponding NEP are 74 V/W and 130 pW/ $\sqrt{\text{Hz}}$  at 400 GHz for room-temperature operation, respectively. Measurement results show that the values of the maximum responsivity of different GFET detectors are fitted with a  $1/n_0$  function with a linear correlation, which provides guidelines for improving the performance of GFET detectors.

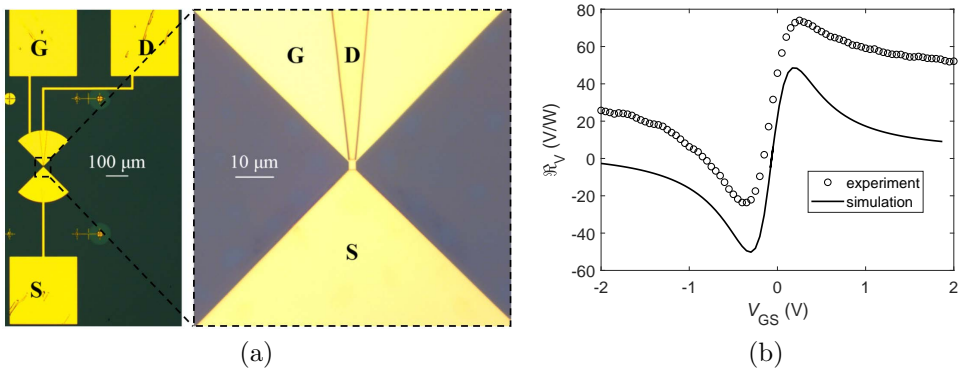


Figure 6.2: (a) Optical micrograph and (b) experimental (symbols) and simulated (solid line) voltage responsivity as a function of gate voltage of the GFET detector in [Paper D] at 400 GHz.



### 6.3 GFET detector on flexible substrate

The unique properties of graphene, such as high carrier mobility [68] and saturation velocity [69], ultra-thin thickness, and outstanding flexibility and stretchability [70], are attractive properties for flexible high-frequency applications. The first terahertz detector based on an antenna-integrated GFET on a flexible substrate is demonstrated in [Paper F], as shown in Figure 6.3.

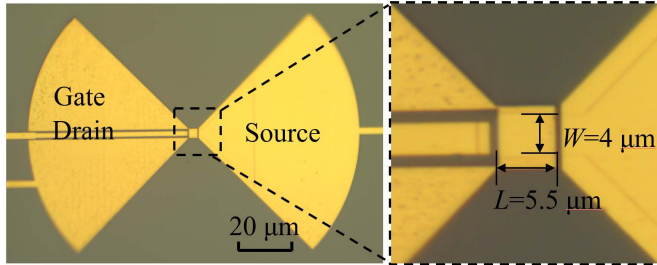


Figure 6.3: Optical micrograph of the GFET detector on a PET substrate in [Paper F].

To investigate the effect of bending strain on the  $I - V$  characteristics and the detector performance, the set of detectors on the PET substrate was mounted on a polytetrafluoroethylene (PTFE) Teflon fixture which has a convex cylindrical surface with the cylinder axis perpendicular to the length of the bow-tie antenna, as shown in Figure 6.4. In this configuration, the detector was located on the outer surface of the bent substrate; hence, it experienced tensile strain in the direction perpendicular to the cylinder axis and corresponding compressive strain along the cylinder axis due to the Poisson effect.

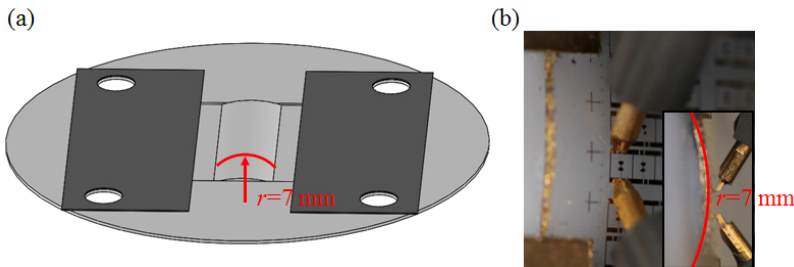


Figure 6.4: (a) schematic image of the PTFE Teflon fixture in [Paper F] for bending test. (b) Photograph of the detector in [Paper F] under test with a bending radius of  $r = 7$  mm, which corresponds to a strain of  $\varepsilon = 1.3\%$ . The inset shows the corresponding side view.

Figures 6.5 (a) and (b) show the voltage responsivity and NEP as a function of gate voltage of the GFET detector in [Paper F] at 487 GHz with different strains, respectively. The solid line represents the simulation results without strain based on the electrical

nonlinear model described in Chapter 3. The detector without strain offers the maximum voltage responsivity above 2 V/W and corresponding NEP below 3 nW/ $\sqrt{\text{Hz}}$  at 487 GHz for room-temperature operation. Based on the bending test results, the voltage responsivity exhibits only a small reduction with increasing strain, which is owing to the excellent mechanical properties of graphene. The effects of bending strain on the performance of GFET detectors are discussed in detail in [Paper F].

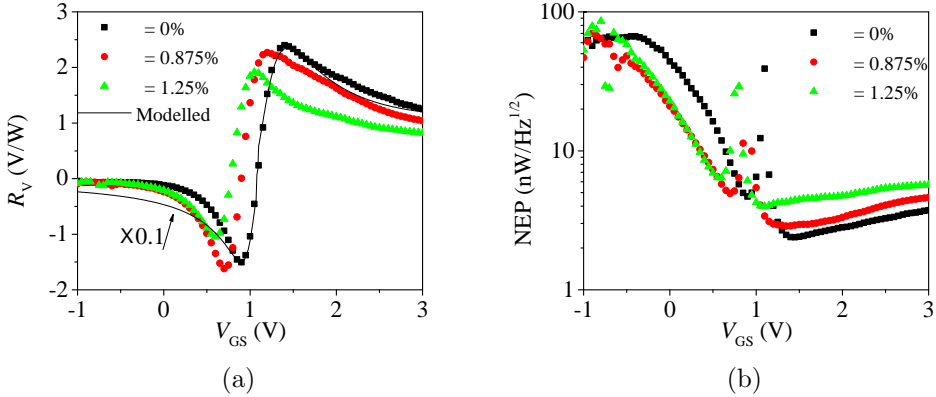


Figure 6.5: Voltage responsivity (a) and NEP (b) as a functions of gate voltage of the GFET detector in [Paper F] at 487 GHz with different strains of 0%, 0.9% and 1.3%. The solid line indicates the modelled results without strain.

## 6.4 GFET detector array on flexible substrate

The development of high-speed terahertz detectors resulted in flat focal-plane arrays being successfully implemented in terahertz imaging [121, 19]. Flat focal-plane arrays based on antenna-coupled direct detectors are demonstrated using semiconductor technologies such as MOSFET [122, 123], HEMT [63], Schottky diode [30], and heterojunction backward diode (HBD) [124]. Compared with flat arrays, curved imaging arrays have the advantages of a larger field of view, better image quality, shape-conforming integration, and simplification of the optical systems. Curved imaging arrays have been demonstrated in the frequency ranges of visible [125, 126] and near-infrared light [20].

A linear array, based on 300-GHz antenna-integrated GFETs on a PEN substrate, is demonstrated in [Paper G]. For bending test, the array sample was mounted and electrically connected to two printed circuit boards (PCBs). Each PCB was attached to a PTFE Teflon beam mounted in a circular trench of a specially designed and in-house fabricated PTFE Teflon fixture, as shown in Figure 6.6 (a). The two PCBs could be tilted by moving the two beams along the circular trench, thus bending the array into a circular arc in a vertical plane, as shown in Figure 6.6 (b).

Figures 6.7 (a) and (b) show the source–drain conductance and the simulated voltage

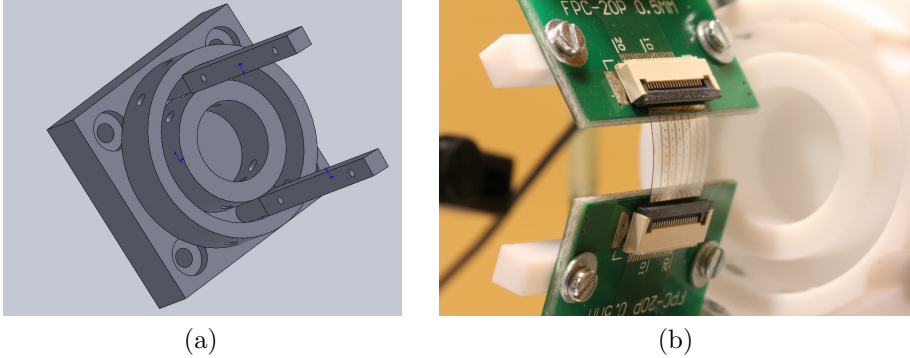


Figure 6.6: (a) Schematic image of the PTFE Teflon fixture in [Paper G] for bending test. (b) Photograph of the set of linear arrays in [Paper G] under test for curved configuration with radius of curvature 13 mm.

responsivity of the  $1 \times 6$  pixel detector array as a function of the gate voltage overdrive from the Dirac point, respectively. The values of conductance for these detectors are in the range of  $0.1 - 0.8$  mS. Similar electrical characteristics are achieved for individual pixels in the detector array. The pixel-to-pixel variations can be associated with both inherent nonuniformities of CVD graphene grown on copper foils, and immature techniques used for fabrication of GFETs and its interfaces.

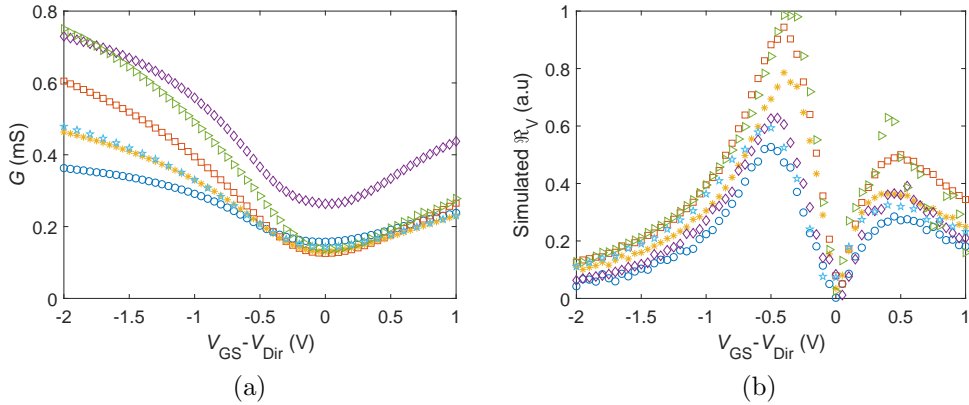


Figure 6.7: (a) Conductance of the pixel detectors as a function of  $V_{GS} - V_{Dir}$  at  $V_{DS} = 1$  mV. (b) Field-effect factor of the pixel detectors.

Figure 6.8 (a) shows the experimental voltage responsivity as a function of frequency. The voltage responsivity at 300 GHz is in the range of  $20 - 70$  V/W, and the corresponding NEP is in the range of  $0.06 - 0.2$  nW/ $\sqrt{\text{Hz}}$  (see [Paper G]). The 300-GHz beam profile at the focal point is shown in Figure 6.8 (b). The profile is nearly Gaussian with a full width

at half maximum (FWHM) around 3 mm, which is much larger than the diameter of the bow-tie antenna ( $d_{\text{ant}} = 300 \mu\text{m}$ ). The half-power beamwidths of the bow-tie antenna radiation pattern are observed to be  $45^\circ$  and  $60^\circ$  for the  $H$ - and  $E$ -planes respectively, which are in good agreement with simulation results. Measurements show that the voltage response for pixels in curved configuration is reduced up to 3 dB due to a decrease of antenna directivity. The array, as a proof of concept, is still limited in size for real applications. However, one can believe that large-scale flexible arrays will become a reality with the advent of graphene growth and GFET fabrication techniques.

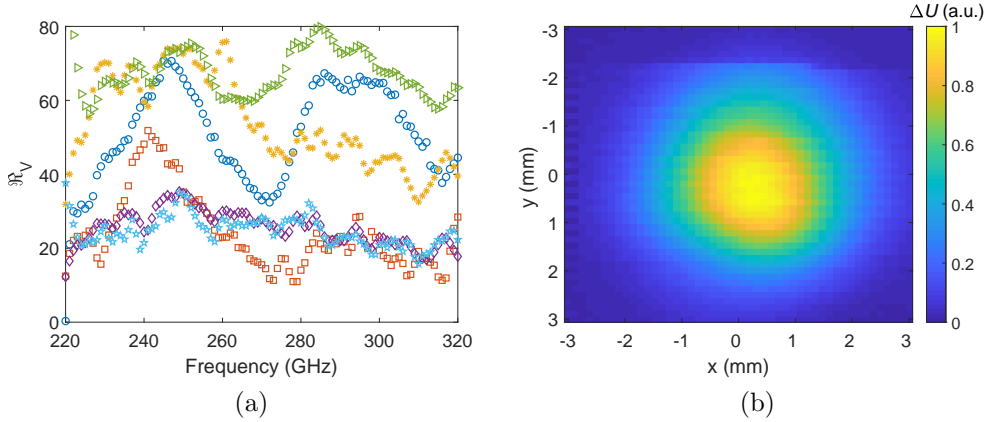


Figure 6.8: (a) Experimental voltage responsivity of the six pixels of the detector array [Paper G] in flat configuration with incident beam normal to each pixel as a function of frequency. (b) 300-GHz beam profile at the focal point of the measurement setup in [Paper G].

# Chapter 7

## Conclusions and future outlook

In this thesis work, modelling, fabrication and characterisation of GFET terahertz detectors were conducted with the aim of developing high-performance detectors for future flexible terahertz electronics.

The modelling and on-wafer characterisation over a wide frequency range indicate that the broadband terahertz response of GFET detectors can be fully described using a combination of a quasi-static equivalent circuit model, and the second-order series expansion terms of the nonlinear dc  $I - V$  characteristic [Paper A]. The method for characterisation and modelling of GFET detectors developed in this work, can generally be applied to any types of power detectors based on non-linear devices.

Measurements of IF bandwidth and low-frequency noise of GFET detectors [Paper B and C] demonstrate the switching speed and  $1/f$  noise characteristics, which is important for future applications of GFETs detectors.

In addition, this study shows that there are mainly five factors affecting the performance of GFET detectors: residual carrier density of graphene, intrinsic gate capacitance and parasitic resistance of transistor, and matching and antenna gain of integrated circuit. By optimising these factors, the results achieved in this study reveal an improvement in terms of responsivity and NEP for GFET detectors, approaching the performance of their semiconductor based counterparts, as shown in Table 7.1.

In the context of these results, advancements in material, design and fabrication techniques are required for further development and optimisation of terahertz detectors based on GFETs. In order to reduce the overall contact resistance, the conventional top-contact design can be replaced by edge-contact with intrinsically lower specific contact resistivity, resulting in performance improvement of GFET detectors. Typically, there is a large density of charged impurities and other defects at the interface between graphene and adjacent dielectrics in GFET structures fabricated by conventional technology. The two-dimensional hexagonal boron nitride (h-BN) encapsulated GFETs with an ultra-flat surface free of dangling bonds and charged impurities can be ideal when reducing the charge carrier scattering, improving the carrier mobility and consequently, improving the performance of terahertz detectors.

Terahertz detectors based on antenna-integrated GFET on have been first demonstrated on plastic substrates [Paper F and G]. The effects of bending strain on dc  $I - V$  characteristics and voltage responsivity have been investigated. This is an important step towards large flexible detector arrays and integrated wearable terahertz sensors, which, in particular, can become an important part of the Internet of things (IoT). For future work, it is interesting to investigate potential applications of GFET terahertz detectors on flexible substrates. Schematic images of a GFET detector array on a plastic substrate and a hemispherical terahertz electronic eye camera based on the array are shown in Figures

Table 7.1: Comparison of room-temperature THz detectors.

Technology	$\Re_V$ (V/W)	NEP (pW/ $\sqrt{\text{Hz}}$ )	Frequency (GHz)	drain/base bias	Ref.
GFET	1800	1000	300	with	Paper A
GFET	300	24	300	without	Paper A
GFET	74	130	400	without	Paper D
GFET	14	515	600	without	Zak, et al. [21]
GFET	0.15	30	300	without	Zak, et al. [21]
AlGaIn/GaN HEMT		25-31	450-650	without	Bauer et al. [61]
AlGaIn/GaN HEMT		30-20	700-900	without	Qin et al. [15]
Si CMOS	5000	10	300	without	Schuster et al. [32]
Si CMOS	1500	15	200	without	Ryu et al. [14]
Schottky diode	400-4000	1.5-15	100-900	without	Hesler et al. [53]
Schottky diode	250	33	280	with	Han et al. [54]
Schottky diode	100	5	100	without	Han et al. [127]
SiGe HBT	6121	21	315	with	Daghestani et al. [56]
Sb-based HBD	2400	2.14	170	without	Rahman et al. [128]

7.1 (a) and (b), respectively. The terahertz camera with simple imaging optics, similar to the structure of biological eyes, can provide a wide field of view and low aberrations, which is difficult to achieve using existing technologies on rigid substrates.

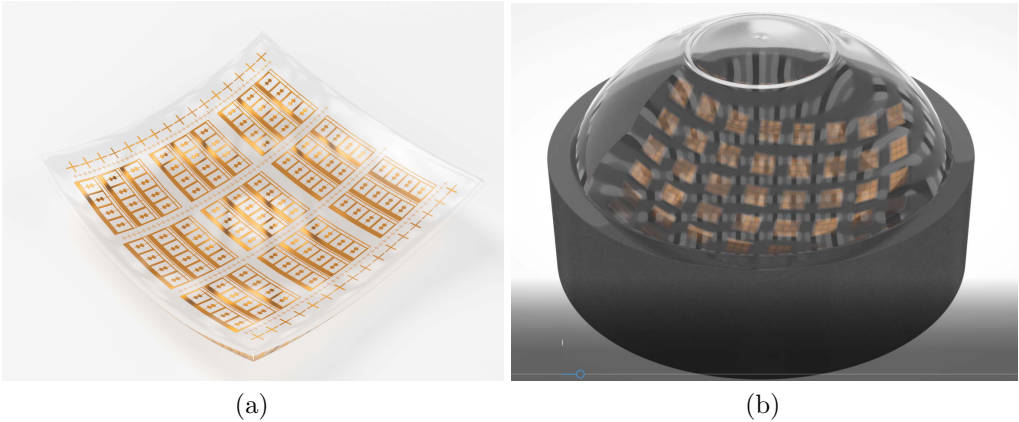


Figure 7.1: Schematic images of a GFET detector array on a plastic substrate (a) and a hemispherical terahertz electronic eye camera based on the array (b).

# Summary of appended papers

## Paper A

**Describing broadband terahertz response of graphene FET detectors by a classical model**

**Xinxin Yang**, Andrei Vorobiev, Kjell Jeppson, and Jan Stake

*IEEE Transactions on Terahertz Science and Technology*, vol. 10, no. 2, 2020. DOI: 10.1109/TTHZ.2019.2960678

The accurate and comprehensive on-wafer characterisation of GFET detectors is demonstrated, which allows for corrections of the impedance mismatch and thereby opens up possibility for detailed measurements up to terahertz frequencies. It is shown that the GFET response versus frequency and bias can be well predicted by a nonlinear empirical model derived from the dc  $I - V$  characteristics and the S-parameters.

*My contributions: Designed, fabricated, and characterised the devices, analysed the results and writing of the paper.*

## Paper B

**Wide bandwidth terahertz mixers based on graphene FETs**

**Xinxin Yang**, Andrei Vorobiev, Kjell Jeppson, Jan Stake, Luca Banszerus, Christoph Stampfer, Martin Otto, and Daniel Neumaier

In *44th International Conference on Infrared, Millimeter, and Terahertz Waves (IRMMW-THz)*, Paris, France, 2019. DOI: 10.1109/IRMMW-THz.2019.8873869

Wide RF and IF bandwidth resistive fundamental terahertz mixers based on graphene field-effect transistors are demonstrated. In the RF frequency range of 220-487 GHz, the 3-dB IF bandwidth is 32 GHz and 56 GHz for the mixers based on graphene field-effect transistors with the gate length of 1.2  $\mu\text{m}$  and 0.6  $\mu\text{m}$ , respectively.

*My contributions: Designed, fabricated and characterised the devices, analysed the results and wrote the paper.*

## Paper C

**Low-frequency noise characterisation of graphene FET THz detectors**

**Xinxin Yang**, Andrei Vorobiev, Kjell Jeppson, Jan Stake, Luca Banszerus, Christoph Stampfer, Martin Otto, and Daniel Neumaier

In *43rd International Conference on Infrared, Millimeter, and Terahertz Waves (IRMMW-*

THz), Nagoya, Japan , 2018. DOI: 10.1109/IRMMW-THz.2018.8510404

The characterisation of the low-frequency noise of graphene field-effect transistor terahertz detectors in the frequency range from 1 Hz to 1 MHz is presented. The room-temperature Hooge parameter is extracted to be around  $2 \times 10^{-3}$ . The voltage responsivity at room-temperature and the corresponding minimum noise equivalent power at 0.3 THz are estimated to be 11 V/W and  $0.2 \text{ nW}/\sqrt{\text{Hz}}$ , respectively, at a modulation frequency of 333 Hz, which shows comparable results with other detector technologies.

*My contributions: Designed, fabricated and characterised the devices, analysed the results and wrote the paper.*

## Paper D

### A 400-GHz graphene FET detector

Andrey A Generalov, Michael A Andersson, **Xinxin Yang**, Andrei Vorobiev, Jan Stake *IEEE Transactions on Terahertz Science and Technology*, vol. 7, no. 5, pp. 614–616, July 2017. DOI: 10.1109/TTHZ.2017.2722360

A high-performance antenna integrated graphene field effect transistor detector is presented. At 400 GHz, the detector reveals a maximum measured optical responsivity of 74 V/W and a minimum noise-equivalent power of  $130 \text{ pW}/\sqrt{\text{Hz}}$ . It is shown, that the detector responsivity increases with decreasing residual carrier density, which is an important material parameter defined by concentration of the charged impurities introduced during the fabrication process.

*My contributions: Participated in the fabrication and characterisation, and provided feedback during the data analysis and paper writing.*

## Paper E

### Test structures for evaluating $\text{Al}_2\text{O}_3$ dielectrics for graphene field effect transistors on flexible substrates

**Xinxin Yang**, Marlene Bonmann, Andrei Vorobiev, Kjell Jeppson, and Jan Stake In *2018 IEEE International Conference on Microelectronic Test Structures (ICMTS)*, Austin, TX, USA, 2018, pp. 75-78. DOI: 10.1109/ICMTS.2018.8383768

Parallel-plate capacitor test structures are developed for evaluating the quality of  $\text{Al}_2\text{O}_3$  gate dielectrics grown on graphene for graphene field effect transistors on flexible substrates. The test structure consists of a metal/dielectric/graphene stack on a PET substrate and requires only one lithography step for the patterning of the topside metal electrodes. Results from measurements of leakage current, capacitance and loss tangent are presented.

*My contributions: Designed, fabricated and characterised the devices, and analysed the results.*



## Paper F

### A flexible graphene terahertz detector

**Xinxin Yang**, Andrei Vorobiev, Andrey A. Generalov, Michael A. Andersson, and Jan Stake

*Applied Physics Letters*, vol. 111, no. 2, pp. 021102-1–021102-4, July 2017. DOI: 10.1063/1.499 3434

The first flexible THz detector based on a CVD graphene field-effect transistor fabricated on a plastic substrate is presented. We have investigated the effects of bending strain on DC characteristics, voltage responsivity and NEP of the detector. The results reveal robust performance of detectors against bending down to radius of 7 mm.

*My contributions: Designed, fabricated and characterised the devices, analysed the results and writing of the paper.*

## Paper G

### A linear-array of 300-GHz antenna integrated GFET detectors on a flexible substrate

**Xinxin Yang**, Andrei Vorobiev, Kjell Jeppson, and Jan Stake

Manuscript submitted as a Letter to *IEEE Transactions on Terahertz Science and Technology*, February, 2020.

A flexible, 300 GHz,  $1 \times 6$  linear detector array based on graphene field-effect transistors and integrated bow-tie antennas is demonstrated. Conservative estimates based on room temperature measurements at 300 GHz indicate the one pixel detector voltage responsivity in the range from 20 V/W to 70 V/W, and noise equivalent powers in the range from 0.06 nW/ $\sqrt{\text{Hz}}$  to 0.2 nW/ $\sqrt{\text{Hz}}$ . Measured radiation patterns, showing good agreement with simulations, reveal half-power beam widths of 45° and 60° for *H*- and *E*-planes, respectively. Characterisation of the antenna array in a curved configuration shows that the voltage response is reduced up to 3 dB compared to the flat configuration due to a decrease of the antenna directivity. We believe that our preliminary results could serve as an enabling platform for future development of flexible antenna arrays based on GFETs for curved focal plane imaging, important for wearable sensors and many other applications.

*My contributions: Designed, fabricated and characterised the devices, analysed the results and writing of the paper.*



# Appendices

## A Fabrication recipe of GFET terahertz detectors on PET substrates

The fabrication process for devices in paper A, which assumes the CVD graphene is transferred onto the PET substrate.

### 1. Protective layer

- Evaporate 1 nm Al, oxidise at room temperature, repeat 2 times.

### 2. Alignment marks

- Spin coat e-beam resist MCC NANO Copolymer EL10 at 3000 rpm during 60 s for 400 nm thickness.
- Soft bake in oven at 110 °C for 10 min.
- Spin coat e-beam resist AR-P 6200.13 diluted 1:2 in anisole at 3000 rpm during 60 s for 95 nm thickness.
- Soft bake in oven at 110 °C for 10 min.
- Evaporate 20 nm Cr.
- E-beam expose pattern proximity corrected using BEAMER at 100 kV/ 10 nA with a dose of 295  $\mu\text{C}/\text{cm}^2$ .
- Remove Cr by chromium etchant diluted 1:2 in deionized water, then rinse off with deionized water, blow-dry by  $\text{N}_2$ .
- Develop AR-P for 45 s in n-Amylacetate, blow-dry by  $\text{N}_2$ .
- Develop copolymer for 2 min in MIBK:IPA 1:1, blow-dry by  $\text{N}_2$ .
- Etch  $\text{Al}_2\text{O}_3$  by buffered oxide etch for 10 s, rinse off with deionized water.
- Etch graphene by oxygen plasma at 50 W RF power and 50 mTorr pressure for 10 s.
- Evaporate 1 nm Ti/ 50 nm Au.
- Lift-off in acetone for 1 h at room temperature, rinse by IPA and deionized water,  $\text{N}_2$  blow dry.

### 3. Mesa isolation

- Spin coat the negative e-beam resist maN 2401 at 3000 rpm during 60 s for 100 nm thickness.
- Soft bake in oven at 110 °C for 3 min.
- Spin coat Spacer 300Z at 1500 rpm during 60 s for 100 nm thickness.

- Soft bake in oven at 110 °C for 3 min.
- E-beam expose pattern proximity corrected using BEAMER at 100 kV/ 2 nA with a dose of 285  $\mu\text{C}/\text{cm}^2$ .
- Remove Spacer with deionized water, then rinse off with deionized water.
- Develop for 30 s in MF-CD-26, rinse by deionized water, blow-dry by  $\text{N}_2$ .
- Etch  $\text{Al}_2\text{O}_3$  by buffered oxide etch for 10 s, rinse off with deionized water.
- Etch graphene by oxygen plasma at 50 W RF power/ 50 mTorr pressure for 10 s.
- Strip resist in acetone for 1 h at room temperature , rinse by IPA and deionized water, blow-dry by  $\text{N}_2$ .

#### 4. Ohmic contact

- Spin coat e-beam resist MCC NANO Copolymer EL10 at 3000 rpm during 60 s for 400 nm thickness.
- Soft bake in oven at 110 °C for 10 min.
- Spin coat AR-P 6200.13 resist diluted 1:2 in anisole at 3000 rpm during 60 s for 95 nm thickness.
- Soft bake in oven at 110 °C for 10 min.
- Evaporate 20 nm Cr.
- E-beam expose pattern proximity corrected using BEAMER at 100 kV/ 10 nA with a dose of 295  $\mu\text{C}/\text{cm}^2$ .
- Remove Cr by chromium etchant diluted 1:2 in deionized water, then rinse off with deionized water, blow-dry by  $\text{N}_2$ .
- Develop AR-P for 45 s in n-Amylacetate, blow-dry by  $\text{N}_2$ .
- Develop copolymer for 2 min in MIBK:IPA 1:1, blow-dry by  $\text{N}_2$ .
- Etch  $\text{Al}_2\text{O}_3$  by buffered oxide etch for 10 s, rinse off with deionized water.
- Evaporate 1 nm Ti/ 5 nm Pd/ 100 nm Au.
- Lift-off in acetone for 1 h at room temperature, rinse by IPA and deionized water, blow-dry by  $\text{N}_2$ .

#### 5. Gate dielectric and electrodes

- Spin coat e-beam resist MCC NANO Copolymer EL10 at 3000 rpm during 60 s for 400 nm thickness.
- Soft bake in oven at 110 °C for 10 min.
- Spin coat AR-P 6200.13 resist diluted 1:2 in anisole at 3000 rpm during 60 s for 95 nm thickness.
- Soft bake in oven at 110 °C for 10 min.
- Evaporate 20 nm Cr.

- E-beam expose pattern proximity corrected using BEAMER at 100 kV/ 10 nA with a dose of  $295 \mu\text{C}/\text{cm}^2$ .
- Remove Cr by chromium etchant diluted 1:2 in deionized water, then rinse off with deionized water, blow-dry by  $\text{N}_2$ .
- Develop AR-P for 45 s in n-Amylacetate, blow-dry by  $\text{N}_2$ .
- Develop copolymer for 2 min in MIBK:IPA 1:1, blow-dry by  $\text{N}_2$ .
- Evaporate 1 nm Al, oxidise at room temperature, repeat 4 times.
- Evaporate 1 nm Ti/ 150 nm Al/ 2 nm Ti/ 150 nm Au.
- Lift-off in acetone for 1 h at room temperature, rinse by IPA and deionized water, blow-dry by  $\text{N}_2$ .

## B Fabrication recipe of GFET terahertz detectors on Si substrates

The fabrication process for devices in paper A, which assumes the CVD graphene is transferred onto the Si/SiO<sub>2</sub> substrate.

### 1. Protective layer

- Evaporate 1 nm Al, oxidise at room temperature, repeat 4 times.

### 2. Alignment marks

- Spin coat e-beam resist MCC NANO Copolymer EL10 at 3000 rpm during 60 s for 400 nm thickness.
- Soft bake on hot-plate at 180 °C for 5 min.
- Spin coat e-beam resist AR-P 6200.13 diluted 1:2 in anisole at 3000 rpm during 60 s for 95 nm thickness.
- Soft bake on hot-plate at 180 °C for 5 min.
- E-beam expose pattern proximity corrected using BEAMER at 100 kV/ 10 nA with a dose of  $360 \mu\text{C}/\text{cm}^2$ .
- Develop AR-P for 45 s in n-Amylacetate, blow-dry by  $\text{N}_2$ .
- Develop copolymer for 2 min in MIBK:IPA 1:1, blow-dry by  $\text{N}_2$ .
- Etch Al<sub>2</sub>O<sub>3</sub> by buffered oxide etch for 10 s, rinse off with deionized water.
- Etch graphene by oxygen plasma at 50 W RF power and 50 mTorr pressure for 10 s.
- Evaporate 15 nm Ti/ 50 nm Au.
- Lift-off in acetone for 1 h at room temperature, rinse by IPA and deionized water,  $\text{N}_2$  blow dry.

### 3. Mesa isolation

- Spin coat the negative e-beam resist maN 2401 at 3000 rpm during 60 s for 100 nm thickness.
- Soft bake on hot-plate at 110 °C for 1 min.
- E-beam expose pattern proximity corrected using BEAMER at 100 kV/ 2 nA with a dose of 320  $\mu\text{C}/\text{cm}^2$ .
- Remove Spacer with deionized water, then rinse off with deionized water.
- Develop for 30 s in MF-CD-26, rinse by deionized water, blow-dry by  $\text{N}_2$ .
- Etch  $\text{Al}_2\text{O}_3$  by buffered oxide etch for 10 s, rinse off with deionized water.
- Etch graphene by oxygen plasma at 50 W RF power/ 50 mTorr pressure for 10 s.
- Strip resist in acetone for 1 h at room temperature , rinse by IPA and deionized water, blow-dry by  $\text{N}_2$ .

#### 4. Ohmic contact

- Spin coat e-beam resist MCC NANO Copolymer EL10 at 3000 rpm during 60 s for 400 nm thickness.
- Soft bake on hot-plate at 180 °C for 5 min.
- Spin coat AR-P 6200.13 resist diluted 1:2 in anisole at 3000 rpm during 60 s for 95 nm thickness.
- Soft bake on hot-plate at 180 °C for 5 min.
- E-beam expose pattern proximity corrected using BEAMER at 100 kV/ 10 nA with a dose of 360  $\mu\text{C}/\text{cm}^2$ .
- Develop AR-P for 45 s in n-Amylacetate, blow-dry by  $\text{N}_2$ .
- Develop copolymer for 2 min in MIBK:IPA 1:1, blow-dry by  $\text{N}_2$ .
- Etch  $\text{Al}_2\text{O}_3$  by buffered oxide etch for 10 s, rinse off with deionized water.
- Evaporate 1 nm Ti/ 5 nm Pd/ 120 nm Au.
- Lift-off in acetone for 1 h at room temperature, rinse by IPA and deionized water, blow-dry by  $\text{N}_2$ .

#### 5. Gate dielectric and electrodes

- Spin coat e-beam resist MCC NANO Copolymer EL10 at 3000 rpm during 60 s for 400 nm thickness.
- Soft bake on hot-plate at 180 °C for 5 min.
- Spin coat AR-P 6200.13 resist diluted 1:2 in anisole at 3000 rpm during 60 s for 95 nm thickness.
- Soft bake on hot-plate at 180 °C for 5 min.
- E-beam expose pattern proximity corrected using BEAMER at 100 kV/ 10 nA with a dose of 360  $\mu\text{C}/\text{cm}^2$ .

- Develop AR-P for 45 s in n-Amylacetate, blow-dry by N<sub>2</sub>.
- Develop copolymer for 2 min in MIBK:IPA 1:1, blow-dry by N<sub>2</sub>.
- Evaporate 1 nm Al, oxidise at room temperature, repeat 6 times.
- Evaporate 1 nm Ti/ 150 nm Al/ 2 nm Ti/ 150 nm Au.
- Lift-off in acetone for 1 h at room temperature, rinse by IPA and deionized water, blow-dry by N<sub>2</sub>.

## 6. Contact pads

- Spin coat e-beam resist MCC NANO Copolymer EL10 at 3000 rpm during 60 s for 400 nm thickness.
- Soft bake on hot-plate at 180 °C for 5 min.
- Spin coat AR-P 6200.13 resist diluted 1:2 in anisole at 3000 rpm during 60 s for 95 nm thickness.
- Soft bake on hot-plate at 180 °C for 5 min.
- E-beam expose pattern proximity corrected using BEAMER at 100 kV/ 35 nA with a dose of 360  $\mu\text{C}/\text{cm}^2$ .
- Develop AR-P for 45 s in n-Amylacetate, blow-dry by N<sub>2</sub>.
- Develop copolymer for 2 min in MIBK:IPA 1:1, blow-dry by N<sub>2</sub>.
- Evaporate 20 nm Ti/ 280 nm Au.
- Lift-off in acetone for 1 h at room temperature, rinse by IPA and deionized water, blow-dry by N<sub>2</sub>.





# Bibliography

- [1] P. H. Siegel, “Terahertz technology,” *IEEE Trans. Microw. Theory Tech.*, vol. 50, no. 3, pp. 910–928, 2002, doi: 10.1109/22.989974.
- [2] T. G. Phillips and J. Keene, “Submillimeter astronomy,” *Proc. IEEE*, vol. 80, no. 11, pp. 1662–1678, 1992, doi: 10.1109/5.175248.
- [3] D. M. Mittleman, “Perspective: Terahertz science and technology,” *J. Appl. Phys.*, vol. 122, no. 23, p. 230901, 2017, doi: 10.1063/1.5007683.
- [4] K. Sengupta, T. Nagatsuma, and D. M. Mittleman, “Terahertz integrated electronic and hybrid electronic–photonic systems,” *Nat. Electron.*, vol. 1, no. 12, pp. 622–635, 2018, doi: s41928-018-0173-2.
- [5] E. Pickwell and V. Wallace, “Biomedical applications of terahertz technology,” *J. Phys. D*, vol. 39, no. 17, p. R301, 2006, doi: 10.1088/0022-3727/39/17/R01.
- [6] K. Kawase, Y. Ogawa, Y. Watanabe, and H. Inoue, “Non-destructive terahertz imaging of illicit drugs using spectral fingerprints,” *Opt. Express*, vol. 11, no. 20, pp. 2549–2554, 2003, doi: 10.1364/OE.11.002549.
- [7] R. Appleby and R. N. Anderton, “Millimeter-wave and submillimeter-wave imaging for security and surveillance,” *Proceedings of the IEEE*, vol. 95, no. 8, pp. 1683–1690, 2007, doi: 10.1109/JPROC.2007.898832.
- [8] T. Kürner and S. Priebe, “Towards THz communications-status in research, standardization and regulation,” *J. Infrared Millim. Terahertz Waves*, vol. 35, no. 1, pp. 53–62, 2014, doi: 10.1007/s10762-013-0014-3.
- [9] R. Lewis, “A review of terahertz detectors,” *J. Phys. D*, vol. 52, no. 43, p. 433001, 2019, doi: 10.1088/0022-3727/47/37/374001.
- [10] M. Tonouchi, “Cutting-edge terahertz technology,” *Nat. Photon.*, vol. 1, no. 2, pp. 97–105, 2007, doi: 10.1038/nphoton.2007.3.
- [11] T. M. Klapwijk and A. Semenov, “Engineering physics of superconducting hot-electron bolometer mixers,” *IEEE Trans. Terahertz Sci. Technol.*, vol. 7, no. 6, pp. 627–648, 2017, doi: 10.1109/TTHZ.2017.2758267.
- [12] L. Liu, J. L. Hesler, H. Xu, A. W. Lichtenberger, and R. M. Weikle, “A broadband quasi-optical terahertz detector utilizing a zero bias Schottky diode,” *IEEE Microw. Wirel. Compon. Lett.*, vol. 20, no. 9, pp. 504–506, 2010, doi: 10.1109/LMWC.2010.2055553.
- [13] V. Vassilev, H. Zirath, R. Kozhuharov, and S. Lai, “140–220-GHz DHBT detectors,” *IEEE Trans. Microw. Theory Tech.*, vol. 61, no. 6, pp. 2353–2360, 2013, doi: 10.1109/TMTT.2013.2259250.

- [14] M. W. Ryu, J. S. Lee, K. S. Kim, K. Park, J.-R. Yang, S.-T. Han, and K. R. Kim, “High-performance plasmonic THz detector based on asymmetric FET with vertically integrated antenna in CMOS technology,” *IEEE Trans. Electron Dev.*, vol. 63, no. 4, pp. 1742–1748, 2016, doi: 10.1109/TED.2016.2526677.
- [15] H. Qin, X. Li, J. Sun, Z. Zhang, Y. Sun, Y. Yu, X. Li, and M. Luo, “Detection of incoherent terahertz light using antenna-coupled high-electron-mobility field-effect transistors,” *Appl. Phys. Lett.*, vol. 110, no. 17, p. 171109, 2017, doi: 10.1063/1.4982604.
- [16] J. Noh, M. Jung, Y. Jung, C. Yeom, M. Pyo, and G. Cho, “Key issues with printed flexible thin film transistors and their application in disposable RF sensors,” *Proc. IEEE*, vol. 103, no. 4, pp. 554–566, 2015, doi: 10.1109/JPROC.2015.2410303.
- [17] X. Huang, T. Leng, M. Zhu, X. Zhang, J. Chen, K. Chang, M. Aqeeli, A. K. Geim, K. S. Novoselov, and Z. Hu, “Highly flexible and conductive printed graphene for wireless wearable communications applications.” *Sci. Rep.*, vol. 5, pp. 18 298–18 298, 2014, doi: 10.1038//srep18298.
- [18] D. Suzuki, S. Oda, and Y. Kawano, “A flexible and wearable terahertz scanner,” *Nat. Photon.*, vol. 10, no. 12, pp. 809–813, 2016, doi: 10.1038/NPHOTON.2016.209.
- [19] P. Hillger, J. Grzyb, R. Jain, and U. R. Pfeiffer, “Terahertz imaging and sensing applications with silicon-based technologies,” *IEEE Trans. Terahertz Sci. Technol.*, vol. 9, no. 1, pp. 1–19, 2018, doi: 10.1109/TTHZ.2018.2884852.
- [20] M. Fendler, D. Dumas, F. Chemla, M. Cohen, P. Laporte, K. Tekaya, E. Le Coarer, J. Primot, and H. Ribot, “Hemispherical infrared focal plane arrays: a new design parameter for the instruments,” in *High Energy, Optical, and Infrared Detectors for Astronomy V*, vol. 8453. International Society for Optics and Photonics, 2012, p. 84531, doi: 10.1117/12.925379.
- [21] A. Zak, M. A. Andersson, M. Bauer, J. Matukas, A. Lisauskas, H. G. Roskos, and J. Stake, “Antenna-integrated 0.6 THz FET direct detectors based on CVD graphene,” *Nano Lett.*, vol. 14, no. 10, pp. 5834–5838, 2014, doi: 10.1021/nl5027309.
- [22] L. Vicarelli, M. Vitiello, D. Coquillat, A. Lombardo, A. Ferrari, W. Knap, M. Polini, V. Pellegrini, and A. Tredicucci, “Graphene field-effect transistors as room-temperature terahertz detectors,” *Nat. Mater.*, vol. 11, no. 10, pp. 865–871, 2012, doi: 10.1038/nmat3417.
- [23] J. Tong, M. Muthee, S.-Y. Chen, S. K. Yngvesson, and J. Yan, “Antenna enhanced graphene THz emitter and detector,” *Nano Lett.*, vol. 15, no. 8, pp. 5295–5301, 2015, doi: 10.1021/acs.nanolett.5b01635.
- [24] D. Spirito, D. Coquillat, S. L. De Bonis, A. Lombardo, M. Bruna, A. C. Ferrari, V. Pellegrini, A. Tredicucci, W. Knap, and M. S. Vitiello, “High performance bilayer-graphene terahertz detectors,” *Appl. Phys. Lett.*, vol. 104, no. 6, p. 061111, 2014, doi: 10.1063/1.4864082.

- [25] F. Bianco, D. Perenzoni, D. Convertino, S. De Bonis, D. Spirito, M. Perenzoni, C. Coletti, M. Vitiello, and A. Tredicucci, "Terahertz detection by epitaxial-graphene field-effect-transistors on silicon carbide," *Appl. Phys. Lett.*, vol. 107, no. 13, p. 131104, 2015, doi: 10.1063/1.4932091.
- [26] Z. Ahmad, A. Lisauskas, H. G. Roskos *et al.*, "9.74-THz electronic far-infrared detection using Schottky barrier diodes in CMOS," in *2014 IEEE International Electron Devices Meeting (IEDM)*. San Francisco, CA, USA: IEEE, 2014, pp. 4–4, doi: 10.1109/IEDM.2014.7046982.
- [27] H. Sherry, R. Al Hadi, J. Grzyb, E. Öjefors, A. Cathelin, A. Kaiser, and U. R. Pfeiffer, "Lens-integrated THz imaging arrays in 65nm CMOS technologies," in *2011 IEEE Radio Frequency Integrated Circuits Symposium (RFIC)*. Baltimore, MD, USA: IEEE, 2011, pp. 1–4, doi: 10.1109/RFIC.2011.5940670.
- [28] J. Sun, Y. Sun, D. Wu, Y. Cai, H. Qin *et al.*, "High-responsivity, low-noise, room-temperature, self-mixing terahertz detector realized using floating antennas on a GaN-based field-effect transistor," *Appl. Phys. Lett.*, vol. 100, no. 1, p. 013506, 2012, doi: 10.1063/1.3673617.
- [29] H. Qin, J. Sun, S. Liang, X. Li, X. Yang, Z. He, C. Yu, and Z. Feng, "Room-temperature, low-impedance and high-sensitivity terahertz direct detector based on bilayer graphene field-effect transistor," *Carbon*, vol. 116, pp. 760–765, 2017, doi: 10.1016/j.carbon.2017.02.037.
- [30] R. Han, Y. Zhang, Y. Kim, D. Y. Kim, H. Shichijo, E. Afshari *et al.*, "Active terahertz imaging using Schottky diodes in CMOS: Array and 860-GHz pixel," *IEEE J. Solid-State Circuits*, vol. 48, no. 10, pp. 2296–2308, 2013, doi: 10.1109/JSSC.2013.2269856.
- [31] R. Al Hadi, H. Sherry, J. Grzyb, N. Baktash, Y. Zhao, E. Öjefors, A. Kaiser, A. Cathelin, and U. Pfeiffer, "A broadband 0.6 to 1 THz CMOS imaging detector with an integrated lens," in *2011 IEEE MTT-S International Microwave Symposium Digest (MTT)*. Baltimore, MD, USA: IEEE, 2011, pp. 1–4, doi: 10.1109/MWSYM.2011.5972870.
- [32] F. Schuster, D. Coquillat, H. Videlier, M. Sakowicz, F. Teppe, L. Dussopt, B. Giffard, T. Skotnicki, and W. Knap, "Broadband terahertz imaging with highly sensitive silicon CMOS detectors," *Opt. Express*, vol. 19, no. 8, pp. 7827–7832, 2011, doi: 10.1364/OE.19.007827.
- [33] R. Tauk, F. Teppe, S. Boubanga, D. Coquillat, W. Knap, Y. Meziani, C. Gallon, F. Boeuf, T. Skotnicki, C. Fenouillet-Beranger *et al.*, "Plasma wave detection of terahertz radiation by silicon field effects transistors: Responsivity and noise equivalent power," *Appl. Phys. Lett.*, vol. 89, no. 25, p. 253511, 2006, doi: 10.1063/1.2410215.
- [34] K. S. Novoselov, A. K. Geim, S. Morozov, D. Jiang, Y. Zhang, S. Dubonos, I. Grigorieva, and A. Firsov, "Electric field effect in atomically thin carbon films," *Science*, vol. 306, no. 5696, pp. 666–669, 2004, doi: 10.1126/science.1102896.

- [35] A. Rogalski, “Graphene-based materials in the infrared and terahertz detector families: a tutorial,” *Adv. Opt. Photonics*, vol. 11, no. 2, pp. 314–379, 2019, doi: 10.1364/AOP.11.000314.
- [36] M. A. Andersson, Y. Zhang, and J. Stake, “A 185–215-GHz subharmonic resistive graphene FET integrated mixer on silicon,” *IEEE Trans. Microw. Theory Tech.*, vol. 65, no. 1, pp. 165–172, 2016, doi: 10.1109/TMTT.2016.2615928.
- [37] B. Sensale-Rodriguez, R. Yan, S. Rafique, M. Zhu, W. Li, X. Liang, D. Gundlach, V. Protasenko, M. M. Kelly, D. Jena *et al.*, “Extraordinary control of terahertz beam reflectance in graphene electro-absorption modulators,” *Nano Lett.*, vol. 12, no. 9, pp. 4518–4522, 2012, doi: 10.1021/nl3016329.
- [38] S. Castilla, B. Terrés, M. Autore, L. Viti, J. Li, A. Y. Nikitin, I. Vangelidis, K. Watanabe, T. Taniguchi, E. Lidorikis *et al.*, “Fast and sensitive terahertz detection using an antenna-integrated graphene pn junction,” *Nano Lett.*, vol. 19, no. 5, pp. 2765–2773, 2019, doi: 10.1021/acs.nanolett.8b04171.
- [39] X. Cai, A. B. Sushkov, R. J. Suess, M. M. Jadidi, G. S. Jenkins, L. O. Nyakiti, R. L. Myers-Ward, S. Li, J. Yan, D. K. Gaskill *et al.*, “Sensitive room-temperature terahertz detection via the photothermoelectric effect in graphene,” *Nat. Nanotechnol.*, vol. 9, no. 10, p. 814, 2014, doi: 10.1038/nnano.2014.182.
- [40] J. Yan, M. H. Kim, J. A. Elle, A. B. Sushkov, G. S. Jenkins, H. M. Milchberg, M. S. Fuhrer, and H. Drew, “Dual-gated bilayer graphene hot-electron bolometer,” *Nat. Nanotechnol.*, vol. 7, no. 7, p. 472, 2012, doi: 10.1038/nnano.2012.88.
- [41] M. A. Andersson and J. Stake, “An accurate empirical model based on volterra series for FET power detectors,” *IEEE Trans. Microw. Theory*, vol. 64, no. 5, pp. 1431–1441, 2016, doi: 10.1109/TMTT.2016.2532326.
- [42] F. Koppens, T. Mueller, P. Avouris, A. Ferrari, M. Vitiello, and M. Polini, “Photodetectors based on graphene, other two-dimensional materials and hybrid systems,” *Nat. Nanotechnol.*, vol. 9, no. 10, p. 780, 2014, doi: /10.1038/nnano.2014.215.
- [43] Z. Popovic and E. N. Grossman, “THz metrology and instrumentation,” *IEEE Trans. Terahertz Sci. Technol.*, vol. 1, no. 1, pp. 133–144, 2011, doi: 10.1109/TTHZ.2011.2159553.
- [44] H. Nyquist, “Thermal agitation of electric charge in conductors,” *Phys. Rev.*, vol. 32, no. 1, p. 110, 1928, doi: 10.1103/PhysRev.32.110.
- [45] G. Hanson and A. Van der Ziel, “Shot noise in transistors,” *Proceedings of the IRE*, vol. 45, no. 11, pp. 1538–1542, 1957, doi: 10.1109/JRPROC.1957.278349.
- [46] F. N. Hooge, “ $1/f$  noise sources,” *IEEE Trans. Electron Devices*, vol. 41, no. 11, pp. 1926–1935, 1994, doi: 10.1109/16.333808.
- [47] J. Sikula and M. Levinshtein, *Advanced experimental methods for noise research in nanoscale electronic devices*. Springer Science & Business Media, 2006, vol. 151.

- [48] D. W. Allan, “Statistics of atomic frequency standards,” *Proceedings of the IEEE*, vol. 54, no. 2, pp. 221–230, 1966, doi: 10.1063/1.3549183.
- [49] P. Richards, “Bolometers for infrared and millimeter waves,” *J. Appl. Phys.*, vol. 76, no. 1, pp. 1–24, 1994, doi: 10.1063/1.357128.
- [50] N. Erickson, “A fast, very sensitive calorimetric power meter for millimeter to sub-millimeter wavelengths,” in *Thirteenth international symposium on space terahertz technology*, 2002.
- [51] V. Desmaris, H. Rashid, A. Pavolotsky, and V. Belitsky, “Design, simulations and optimization of micromachined Golay-cell based THz sensors operating at room temperature,” *Procedia Chemistry*, vol. 1, no. 1, pp. 1175–1178, 2009, doi: 10.1016/j.proche.2009.07.293.
- [52] A. Rogalski, *Infrared detectors*. CRC press, 2010.
- [53] J. L. Hesler and T. W. Crowe, “Responsivity and noise measurements of zero-bias Schottky diode detectors,” *Proc. ISSTT*, pp. 89–92, 2007.
- [54] R. Han, Y. Zhang, D. Coquillat, H. Videlier, W. Knap, E. Brown *et al.*, “A 280-GHz Schottky diode detector in 130-nm digital CMOS,” *IEEE J. Solid-State Circuits*, vol. 46, no. 11, pp. 2602–2612, 2011, doi: 10.1109/JSSC.2011.2165234.
- [55] L. Liu, S. M. Rahman, Z. Jiang, W. Li, and P. Fay, “Advanced terahertz sensing and imaging systems based on integrated III-V interband tunneling devices,” *Proc. IEEE*, vol. 105, no. 6, pp. 1020–1034, 2017, doi: 10.1109/JPROC.2016.2636245.
- [56] D. Yoon, J. Kim, J. Yun, M. Kaynak, B. Tillack, and J.-S. Rieh, “300-GHz direct and heterodyne active imagers based on 0.13- $\mu\text{m}$  SiGe HBT technology,” *IEEE Trans. Terahertz Sci. Technol.*, vol. 7, no. 5, pp. 536–545, 2017, doi: 10.1109/TTHZ.2017.2715419.
- [57] W. Knap, V. Kachorovskii, Y. Deng, S. Rumyantsev, J.-Q. Lü, R. Gaska, M. Shur, G. Simin, X. Hu, M. A. Khan *et al.*, “Nonresonant detection of terahertz radiation in field effect transistors,” *J. Appl. Phys.*, vol. 91, no. 11, pp. 9346–9353, 2002, doi: 10.1063/1.1468257.
- [58] H.-G. Krekels, B. Schiek, and E. Menzel, “Power detector with GaAs field effect transistors,” in *1992 22nd European Microwave Conference*, vol. 1. Helsinki, Finland: IEEE, 1992, pp. 174–179.
- [59] M. Dyakonov and M. Shur, “Detection, mixing, and frequency multiplication of terahertz radiation by two-dimensional electronic fluid,” *IEEE Trans. Electron Devices*, vol. 43, no. 3, pp. 380–387, 1996, doi: 10.1109/16.485650.
- [60] S. Preu, S. Kim, R. Verma, P. Burke, M. Sherwin, and A. Gossard, “An improved model for non-resonant terahertz detection in field-effect transistors,” *J. Appl. Phys.*, vol. 111, no. 2, p. 024502, 2012, doi: 10.1063/1.3676211.

- [61] M. Bauer, A. Ramer, S. A. Chevtchenko, K. Osipov, D. ibiraitė, S. Pralgauskaitė, K. Ikamas, A. Lisauskas, W. Heinrich, V. Krozer *et al.*, “A high-sensitivity AlGaN/GaN HEMT terahertz detector with integrated broadband bow-tie antenna,” *IEEE Trans. Terahertz Sci. Technol.*, vol. 4, no. 4, pp. 430–444, 2019, doi: 10.1109/TTHZ.2019.2917782.
- [62] J. Sun, H. Qin, R. Lewis, Y. Sun, X. Zhang, Y. Cai, D. Wu, and B. Zhang, “Probing and modelling the localized self-mixing in a GaN/AlGaN field-effect terahertz detector,” *Appl. Phys. Lett.*, vol. 100, no. 17, p. 173513, 2012, doi: 10.1063/1.4705306.
- [63] M. Li, X. Lv, J. Mou, D. Guo, H. Qiao, Z. Ma, and H. Hao, “340 GHz lens-coupled 4×4 GaAs detector array for terahertz imaging applications,” *Electron. Lett.*, vol. 54, no. 20, pp. 1180–1182, 2018, doi: 10.1049/el.2018.5856.
- [64] G. Dambrine, A. Cappy, F. Heliodore, and E. Playez, “A new method for determining the FET small-signal equivalent circuit,” *IEEE Trans. Microw. Theory Tech.*, vol. 36, no. 7, pp. 1151–1159, 1988, doi: 10.1109/22.3650.
- [65] D. Costa, W. U. Liu, and J. S. Harris, “Direct extraction of the AlGaAs/GaAs heterojunction bipolar transistor small-signal equivalent circuit,” *IEEE Trans. Electron Devices*, vol. 38, no. 9, pp. 2018–2024, 1991, doi: 10.1109/16.83724.
- [66] J. Gao, X. Li, H. Wang, and G. Boeck, “A new method for determination of parasitic capacitances for PHEMTs,” *Semicond. Sci. Technol.*, vol. 20, no. 6, p. 586, 2005, doi: 10.1088/0268-1242/20/6/018.
- [67] P. R. Wallace, “The band theory of graphite,” *Phys. Rev.*, vol. 71, no. 9, p. 622, 1947, doi: 10.1103/PhysRev.71.622.
- [68] K. I. Bolotin, K. Sikes, Z. Jiang, M. Klima, G. Fudenberg, J. Hone, P. Kim, and H. Stormer, “Ultrahigh electron mobility in suspended graphene,” *Solid State Commun.*, vol. 146, no. 9, pp. 351–355, 2008, doi: 10.1016/j.ssc.2008.02.024.
- [69] R. Shishir and D. Ferry, “Velocity saturation in intrinsic graphene,” *J. Phys. Condens. Matter*, vol. 21, no. 34, p. 344201, 2009, doi: 10.1088/0953-8984/21/34/344201.
- [70] C. Lee, X. Wei, J. W. Kysar, and J. Hone, “Measurement of the elastic properties and intrinsic strength of monolayer graphene,” *Science*, vol. 321, no. 5887, pp. 385–388, 2008, doi: 10.1126/science.1157996.
- [71] Z. Li, E. A. Henriksen, Z. Jiang, Z. Hao, M. C. Martin, P. Kim, H. Stormer, and D. N. Basov, “Dirac charge dynamics in graphene by infrared spectroscopy,” *Nat. Phys.*, vol. 4, no. 7, pp. 532–535, 2008, doi: 10.1038/nphys989.
- [72] A. Kuzmenko, E. Van Heumen, F. Carbone, and D. Van Der Marel, “Universal optical conductance of graphite,” *Phys. Rev. Lett.*, vol. 100, no. 11, p. 117401, 2008, doi: 10.1103/PhysRevLett.100.117401.

- [73] F. Xia, T. Mueller, Y.-m. Lin, A. Valdes-Garcia, and P. Avouris, “Ultrafast graphene photodetector,” *Nat. Nanotechnol.*, vol. 4, no. 12, pp. 839–843, 2009, doi: 10.1038/NNANO.2009.2.
- [74] T. Mueller, F. Xia, and P. Avouris, “Graphene photodetectors for high-speed optical communications,” *Nat. Photonics*, vol. 4, no. 5, pp. 297–301, 2010, doi: 10.1038/NPHOTON.2010.4.
- [75] F. Schwierz, “Graphene transistors,” *Nat. Nanotechnol.*, vol. 5, no. 7, pp. 487–496, 2010, doi: 10.1038/nnano.2010.8.
- [76] V. Ryzhii and M. Ryzhii, “Graphene bilayer field-effect phototransistor for terahertz and infrared detection,” *Phys. Rev. B*, vol. 79, no. 24, p. 245311, 2009, doi: 10.1103/PhysRevB.79.245311.
- [77] X. Xu, N. M. Gabor, J. S. Alden, A. M. van der Zande, and P. L. McEuen, “Photo-thermoelectric effect at a graphene interface junction,” *Nano Lett.*, vol. 10, no. 2, pp. 562–566, 2009, doi: 10.1021/nl903451y.
- [78] M. Dyakonov and M. Shur, “Shallow water analogy for a ballistic field effect transistor: New mechanism of plasma wave generation by dc current,” *Phys. Rev. Letters*, vol. 71, no. 15, p. 2465, 1993, doi: 10.1103/PhysRevLett.71.2465.
- [79] W. Knap, M. Dyakonov, D. Coquillat, F. Teppe, N. Dyakonova, J. Łusakowski, K. Karpierz, M. Sakowicz, G. Valusis, D. Seliuta *et al.*, “Field effect transistors for terahertz detection: Physics and first imaging applications,” *J. Infrared Millim. Terahertz Waves*, vol. 30, no. 12, pp. 1319–1337, 2009, doi: 10.1007/s10762-009-9564-9.
- [80] O. Habibpour, J. Vukusic, and J. Stake, “A large-signal graphene FET model,” *IEEE Trans. Electron Devices*, vol. 59, no. 4, pp. 968–975, 2012, doi: 10.1109/TED.2012.2182675.
- [81] X. Yang, J. Sun, Hua, L. Lv, L. Su, Y. Bo, L. Xinxing, Z. Zhipeng, and F. Jing-Yue, “Room-temperature terahertz detection based on CVD graphene transistor,” *Chin. Phys. B*, vol. 24, no. 4, pp. 047 206(1)–047 206(4), 2015, doi: 10.1088/1674-1056/24/4/047206.
- [82] M. Bonmann, M. Asad, X. Yang, A. Generalov, A. Vorobiev, L. Banszerus, C. Stampfer, M. Otto, D. Neumaier, and J. Stake, “Graphene field-effect transistors with high extrinsic  $f_T$  and  $f_{max}$ ,” *IEEE Electron Device Lett.*, vol. 40, no. 1, pp. 131–134, 2018, doi: 10.1109/LED.2018.2884054.
- [83] G. Gonzalez, *Microwave Transistor Amplifiers (2nd Ed.): Analysis and Design*. USA: Prentice-Hall, Inc., 1996.
- [84] Y. Al-Alem and A. A. Kishk, “Low-profile low-cost high gain 60 GHz antenna,” *IEEE Access*, vol. 6, pp. 13 376–13 384, 2018, doi: 10.1109/ACCESS.2018.2815082.

- [85] S. Adam, E. H. Hwang, V. M. Galitski, and S. D. Sarma, “A self-consistent theory for graphene transport,” *Proc. Natl. Acad. Sci. U.S.A.*, vol. 104, no. 47, pp. 18392–18397, 2007, doi: 10.1073/pnas.0704772104.
- [86] C.-C. Lu, Y.-C. Lin, C.-H. Yeh, J.-C. Huang, and P.-W. Chiu, “High mobility flexible graphene field-effect transistors with self-healing gate dielectrics,” *Acs Nano*, vol. 6, no. 5, pp. 4469–4474, 2012, doi: 10.1021/nm301199j.
- [87] W. A. De Heer, C. Berger, X. Wu, P. N. First, E. H. Conrad, X. Li, T. Li, M. Sprinkle, J. Hass, M. L. Sadowski *et al.*, “Epitaxial graphene,” *Solid State Commun.*, vol. 143, no. 1-2, pp. 92–100, 2007, doi: 10.1016/j.ssc.2007.04.023.
- [88] X. Li, W. Cai, J. An, S. Kim, J. Nah, D. Yang, R. Piner, A. Velamakanni, I. Jung, E. Tutuc *et al.*, “Large-area synthesis of high-quality and uniform graphene films on copper foils,” *Science*, vol. 324, no. 5932, pp. 1312–1314, 2009, doi: 10.1126/science.1171245.
- [89] X. Xu, Z. Zhang, L. Qiu, J. Zhuang, L. Zhang, H. Wang, C. Liao, H. Song, R. Qiao, P. Gao *et al.*, “Ultrafast growth of single-crystal graphene assisted by a continuous oxygen supply,” *Nat. Nanotechnol.*, vol. 11, no. 11, pp. 930–935, 2016, doi: 10.1038/nnano.2016.132.
- [90] A. D. Smith, S. Wagner, S. Kataria, B. G. Malm, M. C. Lemme, and M. Östling, “Wafer-scale statistical analysis of graphene FETs—part i: Wafer-scale fabrication and yield analysis,” *IEEE Trans. Electron Devices*, vol. 64, no. 9, pp. 3919–3926, 2017, doi: 10.1109/TED.2017.2727820.
- [91] E. H. Lock, M. Baraket, M. Laskoski, S. P. Mulvaney, W. K. Lee, P. E. Sheehan, D. R. Hines, J. T. Robinson, J. Tosado, M. S. Fuhrer *et al.*, “High-quality uniform dry transfer of graphene to polymers,” *Nano Lett.*, vol. 12, no. 1, pp. 102–107, 2012, doi: 10.1021/nl203058s.
- [92] X. Liang, B. A. Sperling, I. Calizo, G. Cheng, C. A. Hacker, Q. Zhang, Y. Obeng, K. Yan, H. Peng, Q. Li *et al.*, “Toward clean and crackless transfer of graphene,” *ACS nano*, vol. 5, no. 11, pp. 9144–9153, 2011, doi: 10.1021/nn203377t.
- [93] L. Gao, W. Ren, H. Xu, L. Jin, Z. Wang, T. Ma, L.-P. Ma, Z. Zhang, Q. Fu, L.-M. Peng *et al.*, “Repeated growth and bubbling transfer of graphene with millimetre-size single-crystal grains using platinum,” *Nat. Commun.*, vol. 3, p. 699, 2012, doi: 10.1038/ncomms1702.
- [94] J. Simpson and A. S. Clair, “Fundamental insight on developing low dielectric constant polyimides,” *Thin Solid Films*, vol. 308, pp. 480–485, 1997, doi: 10.1016/S0040-6090(97)00481-1.
- [95] B. Demirel, A. Yaraş, and H. Elçiçek, “Crystallization behavior of PET materials,” *Balikesir Üniversitesi Fen Bilimleri Enstitüsü Dergisi*, vol. 13, no. 1, pp. 26–35, 2016.



- [96] D. Benford, T. Powers, and S. Moseley, “Thermal conductivity of kapton tape,” *Cryogenics*, vol. 39, no. 1, pp. 93–95, 1999, doi: 10.1016/S0011-2275(98)00125-8.
- [97] M. A. Hopcroft, W. D. Nix, and T. W. Kenny, “What is the young’s modulus of silicon?” *J. Microelectromech. Syst.*, vol. 19, no. 2, pp. 229–238, 2010, doi: 10.1109/JMEMS.2009.2039697.
- [98] W. Gao and R. Huang, “Effect of surface roughness on adhesion of graphene membranes,” *J. Phys. D*, vol. 44, no. 45, p. 452001, 2011, doi: 10.1088/0022-3727/44/45/452001.
- [99] M. Ishigami, J. Chen, W. Cullen, M. Fuhrer, and E. Williams, “Atomic structure of graphene on SiO<sub>2</sub>,” *Nano Lett.*, vol. 7, no. 6, pp. 1643–1648, 2007, doi: 10.1021/nl070613a.
- [100] M. von Haartman, A.-C. Lindgren, P. Hellstrom, B. G. Malm, S.-L. Zhang, and M. Ostling, “1/f noise in Si and Si/sub 0.7/Ge/sub 0.3/pMOSFETs,” *IEEE Trans. Electron Devices*, vol. 50, no. 12, pp. 2513–2519, 2003, doi: 10.1109/TED.2003.819258.
- [101] D. Chen and H. Zachmann, “Glass transition temperature of copolyesters of PET, PEN and PHB as determined by dynamic mechanical analysis,” *Polymer*, vol. 32, no. 9, pp. 1612–1621, 1991, doi: 10.1016/0032-3861(91)90396-Z.
- [102] A. Hsu, H. Wang, K. K. Kim, J. Kong, and T. Palacios, “Impact of graphene interface quality on contact resistance and rf device performance,” *IEEE Electron Device Lett.*, vol. 32, no. 8, pp. 1008–1010, 2011, doi: 10.1109/LED.2011.2155024.
- [103] J. A. Robinson, M. LaBella, M. Zhu, M. Hollander, R. Kasarda, Z. Hughes, K. Trumbull, R. Cavalero, and D. Snyder, “Contacting graphene,” *Appl. Phys. Lett.*, vol. 98, no. 5, p. 053103, 2011, doi: 10.1063/1.3549183.
- [104] A. Javey, H. Kim, M. Brink, Q. Wang, A. Ural, J. Guo, P. McIntyre, P. McEuen, M. Lundstrom, and H. Dai, “High- $\kappa$  dielectrics for advanced carbon-nanotube transistors and logic gates,” *Nat. Mater.*, vol. 1, no. 4, pp. 241–246, 2002, doi: 10.1038/nmat769.
- [105] S. M. Sze and K. K. Ng, *Physics of semiconductor devices*. John wiley & sons, 2006.
- [106] V. C. Sundar, J. Zaumseil, V. Podzorov, E. Menard, R. L. Willett, T. Someya, M. E. Gershenson, and J. A. Rogers, “Elastomeric transistor stamps: reversible probing of charge transport in organic crystals,” *Science*, vol. 303, no. 5664, pp. 1644–1646, 2004, doi: 10.1126/science.1094196.
- [107] T.-S. Huang, Y.-K. Su, and P.-C. Wang, “Study of organic thin film transistor with polymethylmethacrylate as a dielectric layer,” *Appl. Phys. Lett.*, vol. 91, no. 9, p. 092116, 2007, doi: 10.1063/1.2775333.

- [108] Y. Kato, S. Iba, R. Teramoto, T. Sekitani, T. Someya, H. Kawaguchi, and T. Sakurai, “High mobility of pentacene field-effect transistors with polyimide gate dielectric layers,” *Appl. Phys. Lett.*, vol. 84, no. 19, pp. 3789–3791, 2004, doi: 10.1063/1.1739508.
- [109] Q. Cao, M.-G. Xia, M. Shim, and J. A. Rogers, “Bilayer organic–inorganic gate dielectrics for high-performance, low-voltage, single-walled carbon nanotube thin-film transistors, complementary logic gates, and p–n diodes on plastic substrates,” *Adv. Funct. Mater.*, vol. 16, no. 18, pp. 2355–2362, 2006, doi: 10.1002/adfm.200600539.
- [110] D. B. Farmer, H.-Y. Chiu, Y.-M. Lin, K. A. Jenkins, F. Xia, and P. Avouris, “Utilization of a buffered dielectric to achieve high field-effect carrier mobility in graphene transistors,” *Nano Lett.*, vol. 9, no. 12, pp. 4474–4478, 2009, doi: 10.1021/nl902788u.
- [111] S. Kim, J. Nah, I. Jo, D. Shahrjerdi, L. Colombo, Z. Yao, E. Tutuc, and S. K. Banerjee, “Realization of a high mobility dual-gated graphene field-effect transistor with  $\text{Al}_2\text{O}_3$  dielectric,” *Appl. Phys. Lett.*, vol. 94, no. 6, p. 062107, 2009, doi: 10.1063/1.3077021.
- [112] M. Groner, J. Elam, F. Fabreguette, and S. M. George, “Electrical characterization of thin  $\text{Al}_2\text{O}_3$  films grown by atomic layer deposition on silicon and various metal substrates,” *Thin Solid Films*, vol. 413, no. 1, pp. 186–197, 2002, doi: 10.1016/S0040-6090(02)00438-8.
- [113] M. Bonmann, A. Vorobiev, J. Stake, and O. Engström, “Effect of oxide traps on channel transport characteristics in graphene field effect transistors,” *J. Vac. Sci. Technol.*, no. 1, p. 01A115, 2017, doi: 10.1116/1.4973904.
- [114] M. Bonmann, M. Krivic, X. Yang, A. Vorobiev, L. Banszerus, C. Stampfer, M. Otto, D. Neumaier, and J. Stake, “Effects of self-heating on  $f_T$  and  $f_{\max}$  performance of graphene field-effect transistors,” *IEEE Trans. Electron Devices*, vol. 67, no. 3, pp. 1277–1284, 2020, doi: 10.1109/TED.2020.2965004.
- [115] M. F. Bauwens, N. Alijabbari, A. W. Lichtenberger, N. S. Barker, and R. M. Weikle, “A 1.1 THz micromachined on-wafer probe,” in *2014 IEEE MTT-S International Microwave Symposium (IMS2014)*. Tampa, FL, USA: IEEE, 2014, pp. 1–4, doi: 10.1109/MWSYM.2014.6848607.
- [116] R. B. Marks, “A multiline method of network analyzer calibration,” *IEEE Trans. Microw. Theory. Tech.*, vol. 39, no. 7, pp. 1205–1215, 1991, doi: 10.1109/22.85388.
- [117] N. M. Ridler, R. G. Clarke, C. Li, and M. J. Salter, “Strategies for traceable submillimeter-wave vector network analyzer,” *IEEE Trans. Terahertz Sci. Technol.*, vol. 9, no. 4, pp. 392–398, 2019, doi: 10.1109/TTHZ.2019.2911870.
- [118] M. Tanzid, M. Andersson, J. Sun, and J. Stake, “Microwave noise characterization of graphene field effect transistors,” *Appl. Phys. Lett.*, vol. 104, no. 1, p. 013502, 2014, doi: 10.1063/1.4861115.

- [119] A. A. Generalov, M. A. Andersson, X. Yang, A. Vorobiev, and J. Stake, “A heterodyne graphene FET detector at 400 GHz,” in *2017 42nd International Conference on Infrared, Millimeter, and Terahertz Waves (IRMMW-THz)*. Cancun, Mexico: IEEE, 2017, pp. 1–2, doi: 10.1109/IRMMW-THz.2017.8067234.
- [120] A. A. Balandin, “Low-frequency  $1/f$  noise in graphene devices,” *Nat. Nanotechnol.*, vol. 8, no. 8, pp. 549–555, 2013, doi: 10.1038/NNANO.2013.1.
- [121] S. van Berkel, O. Yurduseven, A. Freni, A. Neto, and N. Llombart, “THz imaging using uncooled wideband direct detection focal plane arrays,” *IEEE Trans. Terahertz Sci. Technol.*, vol. 7, no. 5, pp. 481–492, 2017, doi: 10.1109/TTHZ.2017.2736338.
- [122] S. Boppel, A. Lisauskas, A. Max, V. Krozer, and H. G. Roskos, “CMOS detector arrays in a virtual 10-kilopixel camera for coherent terahertz real-time imaging,” *Opt. Lett.*, vol. 37, no. 4, pp. 536–538, 2012, doi: 10.1364/OL.37.000536.
- [123] H. Sherry, J. Grzyb, Y. Zhao, R. Al Hadi, A. Cathelin, A. Kaiser, and U. Pfeiffer, “A 1kPixel CMOS camera chip for 25fps real-time terahertz imaging applications,” in *2012 IEEE International Solid-State Circuits Conference (ISSCC)*. San Francisco, CA, USA, 2012, pp. 252–254, doi: 10.1109/ISSCC.2012.6176997.
- [124] G. C. Trichopoulos, H. L. Mosbacker, D. Burdette, and K. Sertel, “A broadband focal plane array camera for real-time THz imaging applications,” *IEEE Trans. Antennas. Propag.*, vol. 61, no. 4, pp. 1733–1740, 2013, doi: 10.1109/TAP.2013.2242829.
- [125] H. C. Ko, M. P. Stoykovich, J. Song, V. Malyarchuk, W. M. Choi, C.-J. Yu, J. B. Geddes Iii, J. Xiao, S. Wang, Y. Huang *et al.*, “A hemispherical electronic eye camera based on compressible silicon optoelectronics,” *Nature*, vol. 454, no. 7205, pp. 748–753, 2008, doi: 10.1038/nature07113.
- [126] S.-B. Rim, P. B. Catrysse, R. Dinyari, K. Huang, and P. Peumans, “The optical advantages of curved focal plane arrays,” *Optics Express*, vol. 16, no. 7, pp. 4965–4971, 2008, doi: 10.1364/OE.16.004965.
- [127] N. Daghestani, K. Parow-Souchon, D. Pardo, H. Liu, N. Brewster, M. Frogley, G. Cinque, B. Alderman, and P. G. Huggard, “Room temperature ultrafast InGaAs Schottky diode based detectors for terahertz spectroscopy,” *Infrared Phys. Technol.*, vol. 99, pp. 240–247, 2019, doi: 10.1016/j.infrared.2019.01.014.
- [128] S. M. Rahman, Z. Jiang, M. I. B. Shams, P. Fay, and L. Liu, “A G-Band monolithically integrated quasi-optical zero-bias detector based on heterostructure backward diodes using submicrometer airbridges,” *IEEE Trans. Microw. Theory Tech.*, vol. 66, no. 4, pp. 2010–2017, 2017, doi: 10.1109/TMTT.2017.2779133.



# Acknowledgements

Time flies! I will soon finish my PhD study in Chalmers, which is and will be forever my extraordinary experience. Looking back to my past life and my study here, I am highly grateful towards the people who work with, help and encourage me to complete my PhD thesis work.

First of all, I would like to express my great gratitude towards my supervisor Prof. Jan Stake for his professional guidance and instruction, which are essential for my PhD work and my future career. Then I would like to express my appreciation towards my co-supervisor Dr. Andrei Vorobiev for a lot of constructive discussions, training, checking my derivations and reviewing my writing.

Moreover, I would like to thank Dr. Michael A. Andersson and Dr. Andrey A. Generalov for helping me with device modelling, fabrication and characterisation, Prof. Kjell Jeppson for helping me acquire critical writing skills, Junjie Li for devoting her mater thesis to noise characterisation, Prof. Serguei Cherednichenko for giving me a lot of advices on measurement setups, Mats Myremark for processing parts of measurement setups, and Muhammad Assad for helping me with device fabrication.

I would like to thank Prof. Jian Yang from antenna research group and his team for collaboration on flexible detector arrays, and Prof. Christoph Stampfer from RWTH Aachen University, Dr. Daniel Neumaier from AMO GmbH and their teams for supplying high-quality graphene.

I would like to thank my previous and current colleagues at TML and MEL, Eunjung Cha, Juan C. Sánchez, Divya Jayasankar, Isabel H. Rodrigues, Anis Moradikouchi, associate Prof. Helena Rodilla, Vladimir Drakinskiy, Dr. Josip Vukusic, Dr. Tomas Bryllert, Prof. Jan Grahn, adjunct Prof. Peter Sobis, Dr. Huan Z. Ternehäll, Dr. Stella Bevilacqua, Johanna Hanning, Nooshien Laderian, Marijana Krivic, Dr. Yu Yan, Dr. Vessen Vassilev, Dr. Zhongxia S. He, Dr. Omid Habibpour, Sining An, Ahmed A. Hassona, Dr. Dhecha Nopchinda and Frida Strömbeck, for their help, support, and accompany during my PhD study.

I am grateful to the staff from Nanofabrication Laboratory for their processing training, and Debora Perlheden for arranging official affairs management.

I will give my special thank to my roommate Dr. Marlene Bonmann and her family Vedad and Ervin, whose accompany will be one of the first things I will miss out of Chalmers.

Finally, thank my husband Xiaolong, my parents, my grandma and my brother Liming.

